Characteristics of Surface "Melt Potential" over Antarctic Ice Shelves based on Regional Atmospheric Model Simulations of Summer Air Temperature Extremes from 1979/80 to 2018/19

Andrew Orr,[a] Pranab Deb,[b] Kyle R. Clem,[c] Ella Gilbert,[a] David H. Bromwich,[d] Fredrik Boberg,[e] Steve Colwell,[a] Nicolaj Hansen,[e,f] Matthew A. Lazzara,[g,h] Priscilla A. Mooney,[i] Ruth Mottram,[e] Masashi Niwano,[j] Tony Phillips,[a] Denys Pishniak,[k] Carleen H. Reijmer,[l] Willem Jan van de Berg,[l] Stuart Webster,[m] and Xun Zou[d,n]

[a] British Antarctic Survey, Cambridge, United Kingdom
[b] Indian Institute of Technology, Kharagpur, India
[c] Victoria University of Wellington, Wellington, New Zealand
[d] Byrd Polar and Climate Research Center, The Ohio State University, Columbus, Ohio
[e] Danish Meteorological Institute, Copenhagen, Denmark
[f] Geodesy and Earth Observation, DTU-Space, Technical University of Denmark, Lyngby, Denmark
[g] University of Wisconsin–Madison, Madison, Wisconsin
[h] Madison Area Technical College, Madison, Wisconsin
[i] NORCE Norwegian Research Centre, Bjerknes Centre for Climate Research, Bergen, Norway
[j] Meteorological Research Institute, Japan Meteorological Agency, Tsukuba, Japan
[k] National Antarctic Scientific Center, Kyiv, Ukraine
[l] Utrecht University, Utrecht, Netherlands
[m] Met Office, Exeter, United Kingdom
[n] Scripps Institution of Oceanography, La Jolla, California

ABSTRACT: We calculate a regional surface "melt potential" index (MPI) over Antarctic ice shelves that describes the frequency (MPI-freq; %) and intensity (MPI-int; K) of daily maximum summer temperatures exceeding a melt threshold of 273.15 K. This is used to determine which ice shelves are vulnerable to melt-induced hydrofracture and is calculated using near-surface temperature output for each summer from 1979/80 to 2018/19 from two high-resolution regional atmospheric model hindcasts (using the MetUM and HIRHAM5). MPI is highest for Antarctic Peninsula ice shelves (MPI-freq 23%–35%, MPI-int 1.2–2.1 K), lowest (2%–3%, <0 K) for the Ronne–Filchner and Ross ice shelves, and around 10%–24% and 0.6–1.7 K for the other West and East Antarctic ice shelves. Hotspots of MPI are apparent over many ice shelves, and they also show a decreasing trend in MPI-freq. The regional circulation patterns associated with high MPI values over West and East Antarctic ice shelves are remarkably consistent for their respective region but tied to different large-scale climate forcings. The West Antarctic circulation resembles the central Pacific El Niño pattern with a stationary Rossby wave and a strong anticyclone over the high-latitude South Pacific. By contrast, the East Antarctic circulation comprises a zonally symmetric negative Southern Annular Mode pattern with a strong regional anticyclone on the plateau and enhanced coastal easterlies/weakened Southern Ocean westerlies. Values of MPI are 3–4 times larger for a lower temperature/melt threshold of 271.15 K used in a sensitivity test, as melting can occur at temperatures lower than 273.15 K depending on snowpack properties.

KEYWORDS: Extreme events; Antarctica; Ice shelves; El Nino; Snowmelt/icemelt; Climate models

1. Introduction

The floating ice shelves that fringe around 75% of Antarctica's coastline have undergone unprecedented thinning and shrinking in recent decades (Paolo et al. 2015). The melting responsible for this can be either from below due to increased incursions of relatively warm water (Pritchard et al. 2012) and/or above due to warming air temperatures (Scambos et al. 2000). In relation to the latter, the presence of substantial surface meltwater ponds is widespread over many Antarctic ice shelves during austral summertime (Luckman et al. 2014; Kingslake et al. 2017; Stokes et al. 2019; Arthur et al. 2020; Dell et al. 2020; Banwell et al. 2021) in response to intense or prolonged surface melting (Trusel et al. 2013; Nicolas et al. 2017; Kuipers Munneke et al. 2018; Johnson et al. 2022). Ensuing vertical fracturing (hydrofracturing) can occur if the meltwater enters downward and enlarges fractures in the ice (Scambos et al. 2000; MacAyeal et al. 2003; Banwell et al. 2013, 2019; Banwell and MacAyeal 2015), potentially triggering their catastrophic collapse (Lai et al. 2020). This has occurred over

---

Corresponding author: Andrew Orr, anmcr@bas.ac.uk

---

several ice shelves on the Antarctic Peninsula in recent decades (Rott et al. 1996; Doake et al. 1998; Scambos et al. 2000, 2009; Glasser et al. 2011).

Ice shelves play an essential role in controlling Antarctic ice sheet stability by restraining (buttressing) the flow of inland ice into the ocean (Rott et al. 1996; Rignot et al. 2019). Their thinning and/or collapse therefore causes acceleration of glacier flow into the ocean, resulting in increased rates of ice sheet mass loss and consequent sea level rise (Pritchard et al. 2012; Rignot et al. 2019). Increased summertime atmospheric warming in the coming decades and centuries will likely result in increased surface melt intensities over many Antarctic ice shelves (Trusel et al. 2015; Chyhareva et al. 2019; Bozkurt et al. 2021; Feron et al. 2021; Gilbert and Kittel 2021; Gutiérrez et al. 2021). This is expected to cause more catastrophic ice shelf collapses like those seen on the Antarctic Peninsula, because other ice shelves could be vulnerable to hydrofracture if inundated with meltwater (Lai et al. 2020). This could prompt significant dynamic destabilization/retreat of the Antarctic ice sheet, accelerating ice loss and sea level rise (DeConto et al. 2021).

Important local scale processes that are associated with warm signatures and ice shelf surface melting include foehn winds (Orr et al. 2008, 2021; Elvidge et al. 2016; Datta et al. 2019; Zou et al. 2021; Gilbert et al. 2022), katabatic winds (Parish and Bromwich 1989; Bromwich et al. 1992; Coggins et al. 2014; Lenaerts et al. 2017; Heinemann et al. 2019), and barrier winds (Orr et al. 2004, 2014; Coggins et al. 2014). Foehn events especially are known to cause extreme temperature increases over a few hours, with temperature spikes in Antarctica of >10 K attributed to them (e.g., Speirs et al. 2010; Bozkurt et al. 2018; Laffin et al. 2021). Relevant synoptic scale processes include warm air intrusions and atmospheric rivers, which can also result in rapid increases in temperature of >10 K and sometimes the co-occurrence of instances of foehn (Nicolas and Bromwich 2011; Nicolas et al. 2017; Bozkurt et al. 2018; Scott et al. 2019; Wille et al. 2019, 2022; Clem et al. 2020; Djoumna and Holland 2021). Additionally, the many synoptic-scale depressions that travel around Antarctica can result in abrupt warming over coastal locations (Simmonds and Keay 2000a; Orr et al. 2014).

Air temperature and melt-related aspects such as liquid-water production are strongly correlated (Ohmura 2001; Hock 2005) and occur in response to a positive surface energy balance when the air/surface temperature is greater than a threshold of 273.15 K (0°C), which is the melting point of ice/snow (Tedesco et al. 2007; Trusel et al. 2012; Barrand et al. 2013; Banwell et al. 2021; Laffin et al. 2021). However, depending on the local properties of the snowpack, melting can also occur at air temperatures lower than 273.15 K. For example, larger snow grains in the snowpack are associated with increased penetration and absorption of solar radiation into the subsurface, enhancing the amount of energy available for melt despite below freezing air temperatures (Liston and Winther 2005; Tedesco 2009; Nicolas et al. 2017). The relationship between air temperatures above any melt threshold and the amount of meltwater produced is also not necessarily linear (Abram et al. 2013; Trusel et al. 2015; Jakobs et al. 2021). For example, melt production is enhanced in regions with relatively low surface albedo due to the associated increased absorption of shortwave radiation increasing the amount of energy available for surface melt (Liston and Winther 2005; Lenaerts et al. 2017; Kingslake et al. 2017). The nonlinear relation between air temperatures and melt is enhanced by melt–albedo feedback, whereby melting causes the snow grain size to increase, lowering the albedo and enhancing melt. This is strongest for low melt rates (<100 mm w.e. yr^{-1}, where w.e. is water equivalent), but weaker for higher melt rates (>200 mm w.e. yr^{-1}) required for ice shelf hydrofracturing (Jakobs et al. 2021).

However, while surface air temperature does not necessarily have a linear relationship with surface melt, it is more reliably simulated by atmospheric models than surface melt (Carter et al. 2022), and therefore it provides a simple and consistent (and less uncertain) measure of "melt potential" that can be compared across all ice shelves and used to identify those that are vulnerable to possible melt-induced hydrofracture. However, the comprehensive understanding of the spatiotemporal characteristics of summertime temperatures over Antarctic ice shelves that is necessary to identify this estimate of melt potential is lacking because 1) in situ meteorological observations are sparse and unevenly distributed and 2) atmospheric models typically lack the requisite fine spatial resolution required to resolve the smaller ice shelves that extend around 50–100 km from the grounding line to the calving front (Deb et al. 2018). Moreover, occurrences of temperature extremes and the local and synoptic meteorological influences and remote effects that can cause them are especially poorly quantified (Wei et al. 2019). Temperature extremes also play an important role in ice shelf surface melt by exceeding the melt threshold for short periods even when average daily temperatures are below freezing and so predict zero melt (van den Broeke et al. 2010; Wei et al. 2019).

Here we address this knowledge deficit by using output from two high horizontal resolution (12 km) regional atmospheric model hindcasts to compute a time series of regional surface melt potential over Antarctic ice shelves based on the occurrence (and magnitude) of temperature extremes for each summer from 1979/80 to 2018/19. We examine variability and trends in this time series, as well as identify regions of potentially enhanced "hotspots." We also examine how its variability is influenced by local and remote atmospheric circulation patterns associated with the Southern Annular Mode (SAM) and El Niño–Southern Oscillation (ENSO). Both these factors have been shown previously to play a key role in driving ice shelf surface melting over Antarctic ice shelves (Nicolas et al. 2017; Deb et al. 2018; Clem et al. 2018; Scott et al. 2019; Johnson et al. 2022).

2. Models, data, and methods

a. Atmospheric models

The two regional atmospheric models used are the U.K. Met Office Unified Model version 11.1 (MetUM) and HIRHAM version 5 (or HIRHAM5). The MetUM model uses the Global Atmosphere 6.0 configuration, which is suitable for the regional configuration of the MetUM at grid scales of 10 km or coarser (Walters et al. 2017). It includes the Even Newer Dynamics for
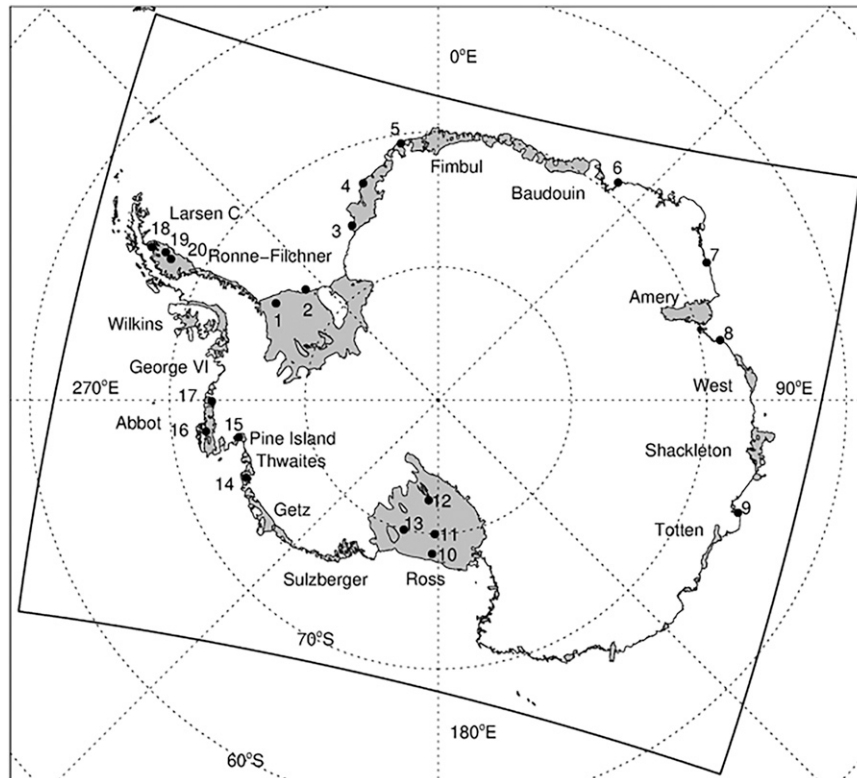
Fig. 1. Map showing the location and names of the 16 ice shelves examined, as well as the locations of the 20 weather stations used (labeled 1–20). The solid box surrounding Antarctica shows the regional domain used by the MetUM and HIRHAM5 simulations. The ice shelves examined are seven in East Antarctica (Ronne–Filchner, Fimbul, Baudouin, Amery, West, Shackleton, Totten), six in West Antarctica (Ross, Sulzberger, Getz, Thwaites, Pine Island, Abbot), and three on the Antarctic Peninsula (George VI, Wilkins, Larsen C).

the General Atmospheric Modeling of the Environment (ENDGame) dynamical core that solves equations for a nonhydrostatic, fully compressible, deep atmosphere. It uses 70 vertical levels in the atmosphere (up to a height of 80 km). The HIRHAM5 model combines the hydrostatic dynamics of the High-Resolution Limited Area Model version 7 (HIRLAM7) and the physical parameterizations of the European Centre Hamburg Model version 5 (ECHAM5) (Christensen et al. 2007). It uses 31 vertical levels in the atmosphere (up to a height of 12.5 hPa). Both models use an ice mask derived from Advanced Very High Resolution Radiometer (AVHRR) data at a resolution of 1 km for the period from 1992 to 1993, although the MetUM ice mask also uses International Geosphere–Biosphere Programme (IGBP) data (Hansen et al. 2022). See Mottram et al. (2021) for further information on the setup and approach used by both models.

The models are 1) run over the standard Antarctic CORDEX domain shown in Fig. 1 for the period from December 1979 through to February 2019 at a grid spacing of 0.11° (~12 km) with the MetUM (HIRHAM5) grid consisting of 392 × 504 (406 × 542) grid points and 2) forced by ERA-Interim reanalysis data (Dee et al. 2011). This yields 40 summer (December–February) melt seasons from 1979/80 to 2018/19. Both hindcasts

are from contributions to the Coordinated Regional Downscaling Experiment (CORDEX; Gutowski et al. 2016), with the high spatial resolution enabling both an improved representation of the local scale processes that impact ice shelf surface melt and coverage of the smaller ice shelves by multiple grid boxes (Deb et al. 2016, 2018; Lenaerts et al. 2018). The HIRHAM5 hindcast uses a long-term continuous integration approach (with no nudging), while the MetUM hindcast uses a frequent reinitialization approach (Lo et al. 2008). The latter consists of a series of twice-daily 24-h forecasts (at 0000 and 1200 UTC), with output at $T + 12$, $T + 15$, $T + 18$, and $T + 21$ h from each of the forecasts concatenated together to form a seamless series of 3-hourly model outputs, with the earlier output discarded as spinup. We use instantaneous 3-hourly outputs of near-surface temperature, which for MetUM is based on 1.5-m air temperature $T_{1.5m}^{MetUM}$, while for HIRHAM5 it is 2-m air temperature $T_{2m}^{HIRHAM5}$.

b. Datasets and climate indices

Summer near-surface temperature measurements with a time resolution of 3-hourly or better are collected from 20 weather stations (6 staffed and 14 automatic) situated either on or close to Antarctic ice shelves (Lazzara et al. 2012). See Fig. 1 for locations. The temperature sensors are located at a standard height

TABLE 1. Details of the 20 weather stations used in the study, showing (from left to right) the number used to label them in Fig. 1 (No.), station name (Station name), latitude and longitude [Lat. (°), Lon. (°)], the number of days of data availability during the study period (No. days), surface type the station is sitting on (Surface type), surface elevation of the station (Elev.), corresponding elevation of MetUM orography (MetUM Elev.), and corresponding elevation of HIRHAM5 orography (HIRHAM5 Elev.). Six of the stations are staffed (specifically Halley, Neumayer, Syowa, Mawson, Davis, and Casey) and the remaining 14 are automatic.

No.	Station name	Lat. (°), Lon. (°)	No. days	Surface type	Elev. (m)	MetUM Elev. (m)	HIRHAM5 Elev. (m)
1	Limbert	−75.87, −59.15	1570	Ice	58	0	0
2	Filchner	−77.07, −50.11	616	Ice	50	0	0
3	Halley	−75.43, −26.22	3555	Ice	30	1.65	0
4	Drescher	−72.87, −19.07	930	Ice	50	0	0
5	Neumayer	−70.67, −8.25	3131	Ice	50	1	0
6	Syowa	−69.00, 39.57	3368	Rock	21	5.8	0
7	Mawson	−67.6, 62.87	3329	Rock	16	165.3	89.0
8	Davis	−68.57, 77.97	3334	Rock	13	15.1	3.0
9	Casey	−66.27, 110.52	2492	Rock	42	56.3	19.3
10	Vito	−78.50, −177.75	1180	Ice	50	0	0
11	Gill	−79.98, −178.57	2877	Ice	54	0	0
12	Lettau	−82.48, −174.59	2368	Ice	38	0	0
13	Margaret	−79.98, −165.10	992	Ice	67	0	0
14	Bear Peninsula	−74.55, −111.88	685	Rock	342	183.0	168.9
15	Evans Knoll	−74.85, −100.40	700	Rock	178	7.5	51.5
16	Thurston Island	−72.53, −97.56	629	Rock	245	225.0	96.8
17	Lepley Nunatak	−73.11, −90.30	599	Rock	159	68.9	20.1
18	Scar Inlet	−65.93, −61.85	390	Ice	50	4.5	0
19	Larsen Ice Shelf	−67.0, −61.47	1868	Ice	43	1.6	0
20	Larsen C South	−67.57, −62.15	483	Ice	50	0.75	0

of >1.5 m and are naturally (wind) ventilated. The temperature measurements are postprocessed to create a time series of observed summer daily maximum temperatures for each station. Any days containing missing data are not included as the maximum value could have occurred at the time corresponding to the missing data. The use of naturally ventilated sensors can result in daytime measured temperatures being warm biased (by up to 10 K) on occasions of high incoming solar radiation and low wind speed (Genthon et al. 2011). However, temperature data from seven of the eight stations located in West Antarctica (Vito, Gill, Lettau, Margaret, Bear Peninsula, Evans Knoll, Thurston Island) were removed if they were thought to be affected by radiation heating effects (Lazzara et al. 2012). Additionally, some of the weather stations are located on rock outcrops, which during summer could also result in warm biased daytime temperatures. Table 1 gives further details of the 20 stations.

The location and geographic extent of the Antarctic ice shelves are based on maps assembled from 2007 to 2009 satellite-based data, which is part of the Making Earth System Data Records for Use in Research Environments (MEaSUREs) program (Mouginot et al. 2017).

We use time series of existing summertime climate indices describing ENSO (Huang et al. 2017a) for the period 1979–2018 based on 1) station-based Southern Oscillation index (SOI) and 2) sea surface temperature (SST) anomalies in the Niño-4 region (5°N–5°S, 160°E–150°W) from the National Oceanic and Atmospheric Administration (NOAA) Optimum Interpolation SST analysis (Huang et al. 2021). Time series of existing summertime climate indices describing the SAM are also used, based on Marshall (2003).

Spatial variability in tropical convection is examined using 1) monthly mean outgoing longwave radiation (OLR) on a 2.5° × 2.5° latitude–longitude grid from the NOAA Interpolated OLR dataset (Liebmann and Smith 1996) and 2) monthly mean SST on a 2° × 2° grid from the NOAA Extended Reconstructed Sea Surface Temperature V5 dataset (Huang et al. 2017b). Variability in the large-scale atmospheric circulation is investigated using several monthly-mean fields from the European Centre for Medium-Range Weather Forecasts (ECMWF) fifth generation atmospheric reanalysis ERA5 (Hersbach et al. 2020), including streamfunction and horizontal wave flux at 200 hPa (Takaya and Nakamura 2001), geopotential height and horizontal wind at 500 hPa, 2-m air temperature, 10-m meridional wind component, and mean sea level pressure (MSLP).

c. Methodology

The 3-hourly values of $T_{1.5m}^{MetUM}$ and $T_{2m}^{HIRHAM5}$ are used to compute a time series of daily maximum temperatures for 40 summer seasons from 1979/80 to 2018/19 for both models. A statistical analysis is made between the model and observed summer daily maximum temperatures for each of the 20 weather station locations, based on mean bias, root-mean-square error (RMSE), and correlation (Deb et al. 2016). Table 1 shows that the number of days of observed summer daily maximum temperatures ranged from a minimum of 390 at Scar Inlet station to a maximum of 3555 at Halley station (and a total of 35 096 days for all 20 stations), i.e., a sufficiently large number to make a robust statistical evaluation. The model-based temperatures at the station locations are computed by bilinear interpolation of the four surrounding grid points. Any adjustment to $T_{1.5m}^{MetUM}$ and

$T_{2m}^{HIRHAM5}$ to account for differences between the actual and model height of the orography are assumed to be small and therefore not included. This assumption is justified as 1) over the ice shelves the difference between the actual and model height is typically less than 100 m (Table 1) and 2) during summer the atmospheric boundary layer over ice shelves is either neutrally or weakly stably stratified, i.e., temperature is only weakly dependent on height (Krinner and Genthon 1999; Kuipers Munneke et al. 2012).

The MetUM and HIRHAM5 time series of summer daily maximum temperatures are used to create a probability distribution function (PDF) at each grid point over an Antarctic ice shelf for each model. We subsequently use these PDFs and the close relationship between air temperature and surface melting (Ohmura 2001; Hock 2005; van den Broeke et al. 2010) to describe an air temperature-based measure of potential melt, which we refer to as the melt potential index (MPI). This is characterized by two components measuring the frequency and intensity of daily maximum temperatures exceeding a temperature/melt threshold value T_0, which we consider to be 273.15 K (0°C). The frequency component (hereafter referred to as MPI-freq) is defined as the percentage of the area under the curve of the PDFs greater than T_0. The intensity component (hereafter referred to as MPI-int) is defined as the difference between the 95th percentile of the distribution of summer daily maximum temperatures and T_0. Essentially these two numbers describe the right-hand-side tail of the PDFs for daily maximum temperatures exceeding the threshold T_0, i.e., conveying physical information such as the likelihood of being exposed to incidences of high melt or low melt. We deliberately calculate MPI based on output from two models to enable model dependence and consistency to be assessed.

Climatological values of MPI-freq and MPI-int (i.e., calculated for all 40 summer seasons) are subsequently computed for 16 individual ice shelves from the daily maximum temperature distribution at each grid point over the ice shelf, with the MEaSUREs dataset used to define the ice shelf areas. Figure 1 shows the locations of the ice shelves selected, consisting of seven in East Antarctica (Ronne–Filchner, Fimbul, Baudouin, Amery, West, Shackleton, Totten), six in West Antarctica (Ross, Sulzberger, Getz, Thwaites, Pine Island, Abbot), and three on the Antarctic Peninsula (George VI, Wilkins, Larsen C). Additionally, climatological values of MPI are computed and mapped for all Antarctic ice shelves to determine localized hotspots.

The MPI for the 16 ice shelves examined is also used to investigate long-term trends and interannual variability. Changepoints in the trends are detected by applying a sequential Mann–Kendall test to the time series (Mann 1945) after a Butterworth low-pass filter has been applied to remove cycles with periodicity > 20 years, with changepoints identified if 1) the time series before and after are statistically significant and 2) the length of the time series on either side of the changepoint is greater than 15 years. Furthermore, the MPI and the various datasets and climate indices are used together with correlation and composite analyses to investigate how remote effects and atmospheric circulation patterns (specially

related to ENSO and SAM) can cause high MPI values over Antarctic ice shelves. Statistical significance of correlations and composite anomalies are calculated using a two-tailed Student's t test, with a confidence interval of 95%.

Finally, as surface melting can occur at air temperatures lower than $T_0 = 273.15$ K, depending on local snowpack properties, we also investigate the sensitivity of MPI to a temperature/melt threshold value of $T_0^S = 271.15$ K (-2.0°C). This value was deemed appropriate by Nicolas et al. (2017) for their study of an extensive summer melt event over the Ross Ice Shelf in West Antarctica. Investigation of a temperature threshold value lower than 273.15 K is further justified as it compensates for both the MetUM and HIRHAM5 models having a cold summer daily maximum temperature bias compared to observations (see below). The results of the sensitivity test are compared against the earlier analysis for $T_0 = 273.15$ K in section 3e.

3. Results

a. Comparison of modeled and observed daily maximum temperatures

When compared to the measured values, the MetUM summer daily maximum temperatures derived from $T_{1.5m}^{MetUM}$ show a cold bias at 15 of the 20 weather station locations, which for 10 stations is less than -1 K (Fig. 2, Table 2). Only Filchner station shows an appreciable warm bias, of 1.6 K. Larger MetUM cold biases of around -2 K are apparent at four sites situated in East Antarctica (Syowa, Mawson, Davis, and Casey), which is perhaps partly related to their location on rock outcrops (Table 1) and the observations suffering from a possible warm bias. MetUM cold biases are also evident for temperatures above $T_0 = 273.15$ K at some sites (e.g., Larsen Ice Shelf, Larsen C South, Drescher; Fig. 2), which is perhaps partly related to daytime measured temperatures being warm biased on occasions of high incoming solar radiation and low wind speed. The RMSE of the MetUM temperatures ranges from 1.58 K (Neumayer) to 3.13 K (Filchner), while the correlation coefficient ranges from 0.62 (Larsen Ice Shelf) to 0.91 (Lettau and Margaret). The HIRHAM5 summer daily maximum temperatures derived from $T_{2m}^{HIRHAM5}$ typically have a larger cold bias, larger RMSE, and lower correlation than the MetUM results (Fig. 2, Table 2). A much larger cold bias (up to -4.43 K) in the HIRHAM5 temperatures is especially evident at sites located on Ross (Vito, Gill, Lettau, and Margaret) and Ronne–Filchner (Limbert). This result is also consistent with Mottram et al. (2021), which showed that both models were characterized by a distinct cold bias when compared with daily observations across Antarctica. This temperature bias is a combination of measurement error and model deficiencies, with the latter of these most likely the main cause of the bias. Previous studies have shown that known deficiencies in the cloud scheme used by these models lead to considerable biases in the surface energy balance and near-surface temperature (Wilson et al. 2012; van Wessem et al. 2014). For example, in Antarctica the single-moment cloud scheme used by the MetUM is characterized by clouds containing too
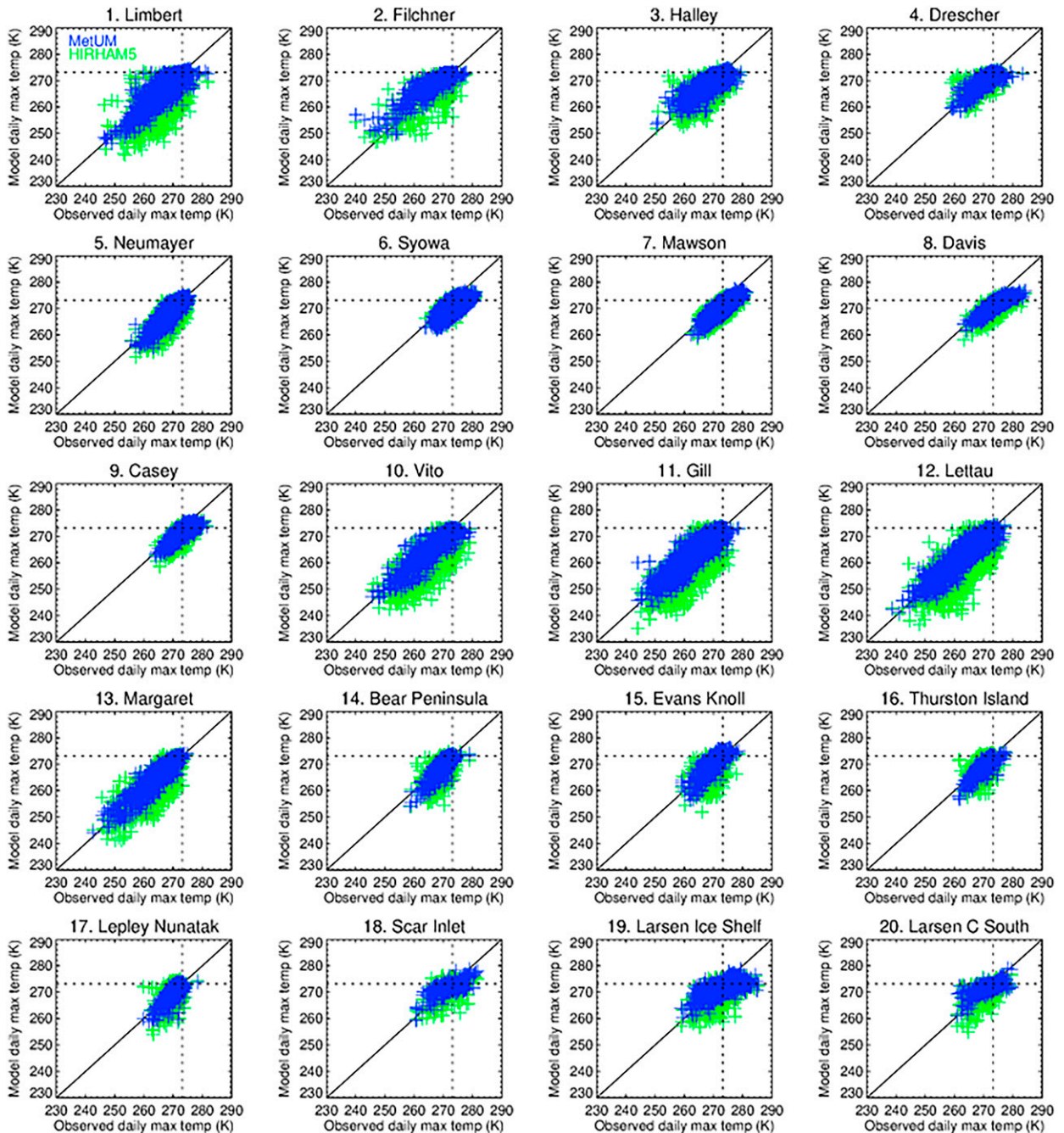
FIG. 2. Scatterplots comparing the observed daily maximum temperature and MetUM (blue) and HIRHAM5 (green) model daily maximum temperature at each of the 20 weather stations shown in Fig. 1 and listed in Table 1. The dashed lines show the temperature/melt threshold value $T_0 = 273.15$ K.

much ice and not enough liquid water (Abel et al. 2017), which influences the downwelling radiative fluxes enough to affect surface melting (King et al. 2015; Gilbert et al. 2020, 2022).

Nevertheless, the relatively good performance of the MetUM suggests that PDFs of daily maximum temperatures over Antarctic ice shelves derived from its output are broadly representative of actual conditions, which gives us confidence that the derived MPI are physically realistic; much of our ensuing investigation will therefore focus on analysis of the MetUM results. However, the MPI derived from the HIRHAM5 output are still important as they enable the dependency/consistency between models and robustness of the findings to be assessed (Gutowski et al. 2016).

TABLE 2. Statistical analysis of the model-based summer daily maximum temperatures at the 20 weather stations used in the study, showing the number used to label each site in Fig. 1 (No.), the station name (Station name), root-mean-square error (RMSE), bias (BIAS), and correlation (CORR). In the final three columns of the table, the MetUM results are given first and the HIRHAM5 results second (i.e., MetUM, HIRHAM5).

		Daily maximum temperature (MetUM, HIRHAM5)		
No.	Station name	RMSE (K)	BIAS (K)	CORR
1	Limbert	2.68, 5.83	−0.29, −3.03	0.87, 0.69
2	Filchner	3.13, 4.38	1.57, −0.75	0.89, 0.72
3	Halley	1.93, 2.97	0.09, −1.06	0.82, 0.66
4	Drescher	1.93, 2.72	−0.54, −0.97	0.79, 0.61
5	Neumayer	1.58, 3.07	−0.05, −1.69	0.87, 0.75
6	Syowa	2.92, 2.51	−2.25, −1.90	0.68, 0.73
7	Mawson	2.95, 3.45	−2.64, −2.95	0.87, 0.77
8	Davis	2.97, 3.87	−2.63, −3.40	0.87, 0.74
9	Casey	2.18, 2.62	−1.75, −1.98	0.83, 0.75
10	Vito	2.53, 6.35	−0.67, −4.43	0.90, 0.73
11	Gill	2.37, 5.62	−0.14, −3.67	0.90, 0.76
12	Lettau	2.40, 6.07	−0.33, −4.19	0.91, 0.76
13	Margaret	2.39, 5.00	0.66, −2.56	0.91, 0.75
14	Bear Peninsula	2.03, 3.58	−0.59, −1.43	0.82, 0.58
15	Evans Knoll	2.02, 3.88	0.39, −1.23	0.83, 0.57
16	Thurston Island	1.82, 3.24	−0.84, −0.82	0.82, 0.51
17	Lepley Nunatak	1.88, 3.29	−0.21, −0.47	0.78, 0.49
18	Scar Inlet	2.56, 3.29	−0.38, −1.20	0.71, 0.62
19	Larsen Ice Shelf	2.92, 3.63	−1.28, −2.12	0.62, 0.57
20	Larsen C South	2.28, 3.12	0.24, −1.00	0.72, 0.62

b. Hotspots of melt potential

Figure 3 shows that the MetUM and HIRHAM5 climatological PDFs of summer daily maximum temperatures for the 16 ice shelves investigated are broadly similar, i.e., the consistency between models is evidence that the results are robust. The associated values of MPI-freq and MPI-int for each ice shelf for a temperature/melt threshold of $T_0 = 273.15$ K are shown in Table 3 (as well as displayed on Fig. 3). The PDFs for 14 of the 16 ice shelves show a peak occurring for temperatures around T_0 (the exception being Ronne–Filchner and Ross). Based on MetUM output, MPI-freq (i.e., the area of the PDF exceeding T_0) is highest for George VI, Wilkins, and Larsen C on the Antarctic Peninsula (23%–35%), lowest for Ronne–Filchner and Ross (2%–3%), and between 10% and 24% for the other West and East Antarctic ice shelves (23.7% for Pine Island). Values of MPI-freq based on HIRHAM5 output broadly agree with the MetUM values for most of the ice shelves, except for George VI (44.7% for HIRHAM5 compared to 30.4% for MetUM) and Wilkins (44.6% compared to 34.8%). Some of the highest values of MetUM MPI-int are for George VI (2.1 K), Wilkins (1.5 K), and Larsen C (1.2 K) (Table 3), while the lowest are for Ronne–Filchner and Ross (<0 K). For East Antarctica, MPI-int ranges from 0.6 to 1.2 K (excluding Ronne–Filchner), while for West Antarctica it is around 0.8 K (excluding Ross and Pine Island). The value for Pine Island (1.7 K) is the highest outside of the Antarctic Peninsula and suggests that this ice shelf is vulnerable to extreme surface melt events in addition to the well-known basal melting (Jenkins et al. 2010, 2016). The HIRHAM5 MPI-int values are similar to the MetUM for 9 of the 16 ice shelves (with the exception of Ronne–Filchner, Amery, Pine Island, and George VI, which are lower in HIRHAM5, and Ross, Wilkins, and Larsen C, which are higher).

Figure 3 also shows the PDFs of summer daily average temperature (dashed lines), which for many of the ice shelves are primarily determined by climatological factors like latitude and insolation. For many of the ice shelves, this curve shows a peak that occurs at roughly the same temperature as the peak in daily maximum temperature (solid lines). The high values of MPI-freq and MPI-int for Larsen C and Wilkins (23.0% and 1.2 K for Larsen C and 34.8% and 1.5 K for Wilkins, based on MetUM) are consistent with these being some of the warmest regions of Antarctica. In the case of Larsen C this is due to its location being relatively far north (so higher insolation during summer) and from the frequent occurrence of warm foehn winds (Orr et al. 2008; Elvidge et al. 2016; Datta et al. 2019; Gilbert et al. 2022). For Wilkins its location on the western coast of the Peninsula means it is strongly influenced by the circumpolar westerly flow around Antarctica, which is blocked by the high orography of the Peninsula and deflected to the right, resulting in relatively warm maritime northerly winds over Wilkins (Orr et al. 2004). By contrast, the low values of MPI-freq and MPI-int for Ronne–Filchner (2.6% and −0.3 K, based on MetUM) and Ross (2.3% and −0.7 K) are consistent with these ice shelves extending far to the south and therefore some of the coldest regions considered, meaning that summer daily maximum (and average) temperatures are typically below $T_0 = 273.15$ K (Costanza et al. 2016; Jakobs et al. 2021).

To map localized hotspots of MPI, Fig. 4 shows the spatial pattern of climatological values of MPI-freq and MPI-int for a temperature/melt threshold of $T_0 = 273.15$ K over all Antarctic ice shelves. The MetUM MPI-freq (Fig. 4a) shows that the highest values are again found on the Antarctic Peninsula, which are around 30% over the northern section of Larsen C and around 40% along its western coast. This is followed by West Antarctica and the region of East Antarctica east of Amery (ranging from 10% to 30%), then the region of East Antarctica to the west of Amery (ranging from 0% to 20%), and finally Ross and Ronne–Filchner (0%–10%). The Ross, Ronne–Filchner, and Larsen C are sufficiently large to show a latitudinal gradient in MPI-freq, which is consistent with the broadscale latitudinal insolation gradient. Additionally, regional differences in MPI-freq are apparent between ice shelves located at similar latitudes in both West and East Antarctica. In West Antarctica, MPI-freq is higher over ice shelves located in eastern sectors compared to western sectors, which is consistent with the climatological influence of the Amundsen Sea low on temperatures (Hosking et al. 2013; Scott et al. 2019). In the region of East Antarctica to the west of Amery, MPI-freq is also higher over ice shelves located in eastern sectors compared to western sectors, which is consistent with the influence of the climatological zonal wavenumber-3 pattern (Goyal et al. 2021).
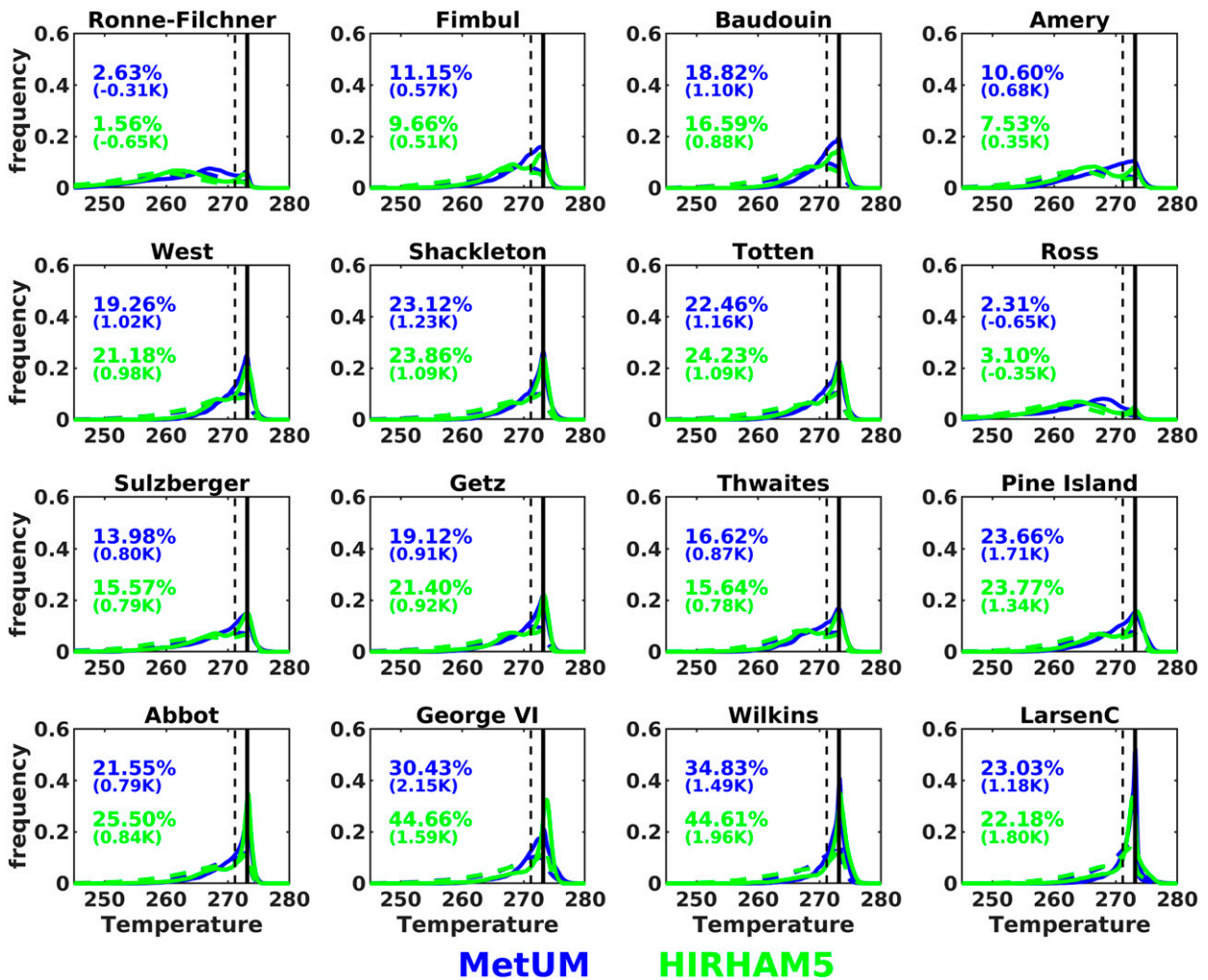
FIG. 3. Probability distribution functions (PDFs) of summer daily maximum near-surface temperature for 16 Antarctic ice shelves (solid lines) based on MetUM (blue) and HIRHAM5 (green) output. The numbers show climatological values of MPI-freq (%) and MPI-int (K; shown in parentheses) calculated from these distributions for a temperature/melt threshold of $T_0 = 273.15$ K (shown as the vertical solid line). Values of MPI-freq and MPI-int are shown for both MetUM (blue) and HIRHAM5 (green). These numbers are also shown in Table 3. Also shown are the PDFs of summer daily mean temperature (dashed lines). The ice shelves examined are (from top left to bottom right) Ronne–Filchner, Fimbul, Baudouin, Amery, West, Shackleton, Totten, Ross, Sulzberger, Getz, Thwaites, Pine Island, Abbot, George VI, Wilkins, and Larsen C. The dashed vertical line shows the temperature/melt threshold value of $T_0^S = 271.15$ K used in the sensitivity test.

Hotspots of MetUM MPI-freq are particularly apparent over Amery, Ross, and Ronne–Filchner. The Amery ice shelf is characterized by increased values over its southern and northern edges of 10%–20% (resulting in a minimum over its central section), with the high values over the southern edge likely caused by the pronounced funneling of katabatic winds that occurs here and the associated warming (Parish and Bromwich 1991). Katabatic winds can cause warming through increased mixing in the stable boundary layer resulting in relatively warmer air from aloft being mixed to the surface, as well as by adiabatic warming (Parish and Bromwich 1989; Bromwich et al. 1992; Heinemann et al. 2019). The Ross ice shelf has increased MPI-freq of 5%–10% along its southern and western sectors bordering the Transantarctic Mountains, which is probably associated with the southerly surface wind regime in this region referred to as the Ross Ice Shelf air stream (Seefeldt and Cassano 2012). This is made up of interactions between barrier winds and katabatic winds and synoptic forcing from cyclonic systems in the Ross Sea (Parish et al. 2006), and has a marked warming effect on the surface of Ross (Coggins et al. 2014). Additionally, a narrow region of high MPI-freq of around 10% exists along the eastern section of Ross. This is probably associated with the frequent occurrence of foehn winds in this region, which are associated with localized warming that has been shown to cause surface melting (Zou et al. 2021). For Ronne–Filchner, relatively high MPI-freq of around 10% occurs over its western margins, which is likely related to synoptic conditions (Scott et al. 2019), i.e., many of the atmospheric circulation patterns that

TABLE 3. Climatological values of MPI-freq (second column) and MPI-int (third column) for the 16 ice shelves examined for a temperature/melt threshold of $T_0 = 273.15$ K. Results based on MetUM output are shown first and HIRHAM5 output second (i.e., MetUM, HIRHAM5). These values are also shown in Fig. 3. Columns four and five show analogous results for the sensitivity test using a temperature/melt threshold value of $T_0^S = 271.15$ K.

Ice shelf	$T_0 = 273.15$ K (MetUM, HIRHAM5)		$T_0^S = 271.15$ K (MetUM, HIRHAM5)	
	MPI-freq (%)	MPI-int (K)	MPI-freq (%)	MPI-int (K)
Ronne–Filchner	2.6, 1.6	−0.3, −0.7	13.2, 10.4	1.7, 1.4
Fimbul	11.2, 9.7	0.6, 0.5	41.0, 31.9	2.7, 2.5
Baudouin	18.8, 16.7	1.1, 0.9	53.5, 42.9	3.1, 2.9
Amery	10.6, 7.5	0.7, 0.4	30.9, 20.4	2.7, 2.4
West	19.3, 21.2	1.0, 1.0	57.0, 51.3	3.0, 3.0
Shackleton	23.1, 23.9	1.2, 1.1	59.2, 55.5	3.2, 3.1
Totten	22.5, 24.2	1.1, 1.1	56.0, 52.6	3.2, 3.1
Ross	2.3, 3.1	−0.7, −0.4	10.4, 10.0	1.4, 1.7
Sulzberger	14.0, 15.6	0.8, 0.8	40.4, 38.6	2.8, 2.8
Getz	19.1, 21.4	0.9, 0.9	52.1, 48.0	2.9, 2.9
Thwaites	16.6, 15.6	0.9, 0.8	44.0, 38.3	2.9, 2.8
Pine Island	23.7, 23.8	1.7, 1.3	49.5, 44.0	3.7, 3.3
Abbot	21.6, 25.5	0.8, 0.8	56.9, 57.0	2.8, 2.8
George VI	30.4, 44.7	2.1, 1.6	63.3, 70.2	4.2, 3.6
Wilkins	34.8, 44.6	1.5, 2.0	75.3, 75.7	3.5, 4.0
Larsen C	23.0, 22.2	1.2, 1.8	74.3, 68.3	3.2, 3.8

cause surface melting and anomalously warm near-surface temperatures over West Antarctica also affect Ronne–Filchner. For example, one of the patterns Scott et al. (2019) identify (labeled synoptic pattern 8) is related to a ridge over the Antarctic Peninsula, which promotes warm marine air intrusions from the Bellingshausen Sea onto eastern parts of West Antarctica (Ellsworth Land) that travel as far as Ronne–Filchner. High MPI-freq in this location could also be aided by foehn winds in the lee of the Ellsworth Mountains (>4500-m elevation) and southern section of the Antarctic Peninsula (Palmer Land).

The MetUM MPI-int varies from 0 to 2.5 K (Fig. 4c). The higher values (around 2.5 K) are found over the northern sections of Larsen C, the western coast of the Antarctic Peninsula, and Pine Island, as well as a few other isolated and localized areas. Additionally, there are amplified values of MPI-int along the western margins of Larsen C, which is consistent with the frequent occurrence of warm foehn winds in this region (Orr et al. 2008; Luckman et al. 2014; Elvidge et al. 2016; Datta et al. 2019; Gilbert et al. 2022). Furthermore, MPI-int (and MPI-freq) values are often largest over the region of the ice shelf nearest the slopes of the ice sheet for many Antarctic ice shelves, which again is likely explained by katabatic warm signatures. This is especially apparent over the katabatic wind confluence zones in East Antarctica (Parish and Bromwich 1991), which show MPI-int values of 1–1.5 K. Katabatic outflows and their accompanying warm signatures can extend more than 100 km over flat ice shelves, and even further if favorable synoptic conditions are present that cause katabatic surges (Bromwich et al. 1992; Heinemann et al. 2019). The lower values of MetUM MPI-int occur over Ronne–Filchner and the central sector of Ross. However, values of MPI-int are up to 1 K higher over the southern and eastern sections of the Ross, which are also likely associated with the warming effects associated with the Ross Ice Shelf air

stream and foehn winds, as well as katabatic outflows (Bromwich et al. 1992; Coggins et al. 2014; Zou et al. 2021). For Ronne–Filchner, values of MP-int are higher over its western margins, which is likely related to synoptic conditions (Scott et al. 2019).

Examination of HIRHAM5 MPI-freq (Fig. 4b) and MPI-int (Fig. 4d) shows that they are broadly consistent with the MetUM results. Although it is noticeable that MPI-freq values over the western coast of the Antarctic Peninsula are larger in HIRHAM5 compared to MetUM, while those for Amery and the region of East Antarctica to the west of Amery are smaller. Additionally, HIRHAM5 MPI-int appear less locally detailed in some regions compared to MetUM values. In particular, the high MPI-int values near the slopes of the ice sheet are less apparent in the HIRHAM5 results (especially around East Antarctica), suggesting that a key difference in the models may be in their representation of katabatic winds and their flow over the ice shelves (Orr et al. 2014; Heinemann et al. 2019). Differences in the representation of foehn winds could also be responsible for some of the differences in MPI-int for Larsen C, the eastern sector of Ross, and the western sector of Ronne–Filchner.

c. Trends and interannual variability of melt potential

Figure 5 shows the time series of MetUM and HIRHAM5 MPI-freq for a temperature/melt threshold of $T_0 = 273.15$ K for the 16 ice shelves, including the linear trend for the period and any changepoints in the trend (Tables 4 and 5). The interannual variability and linear trends are broadly similar between models. Many of the ice shelves are characterized by a relatively high interannual variability. For West Antarctic and Antarctic Peninsula ice shelves, this is consistent with the high variability of the Amundsen Sea Low that controls much of the climatic variability in this region (Hosking et al. 2013; Scott et al. 2019). For East Antarctica ice shelves, this is
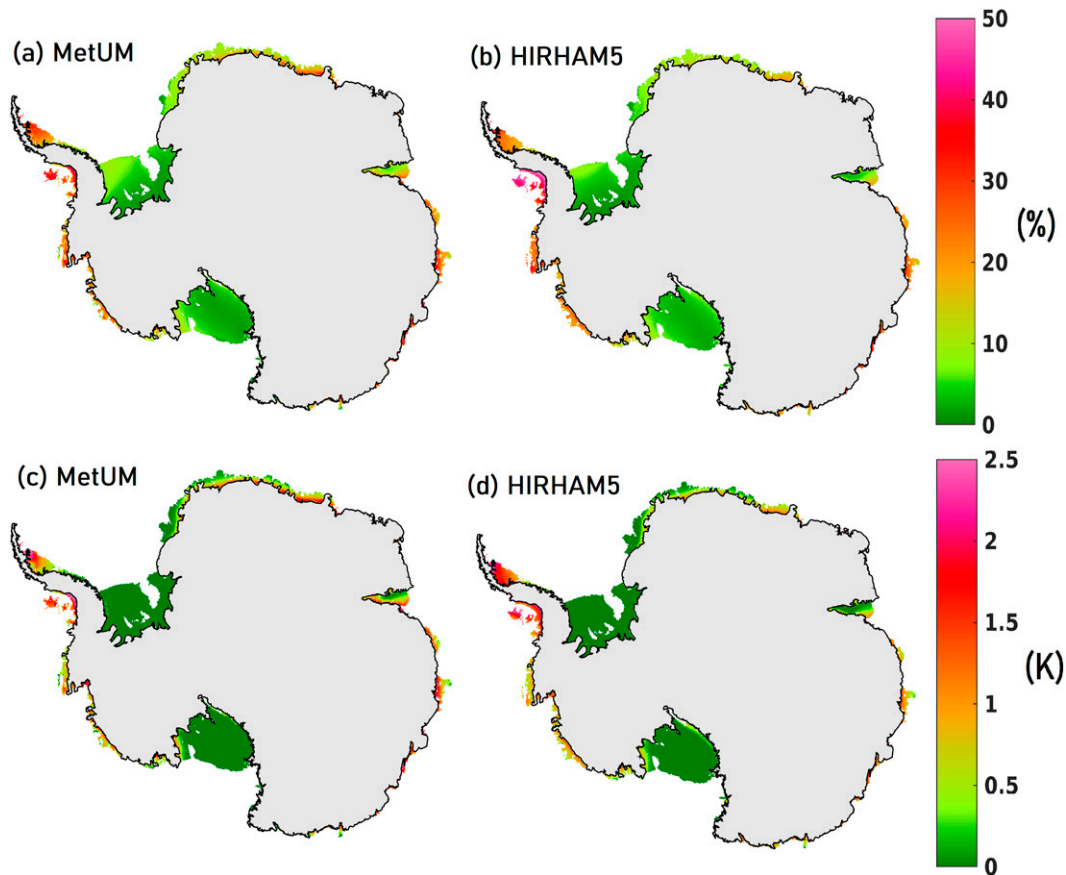
FIG. 4. Maps of the climatological values of (top) MPI-freq and (bottom) MPI-int for a temperature/melt threshold of $T_0 = 273.15$ K based on (left) MetUM and (right) HIRHAM5 output.

consistent with the large interannual variability in cyclone frequency (Simmonds and Keay 2000b). However, interannual variability would also be influenced by local processes driving temperature extremes, as well as specific atmospheric circulation features. By contrast, Ross and Ronne–Filchner have a relatively small range of interannual variability, which is perhaps because these are much larger ice shelves and so any averaged quantity is somewhat smoothed. The MetUM MPI-freq for many of the ice shelves in West Antarctica (Getz, Thwaites, Pine Island, Abbot), East Antarctica (Ronne–Filchner, Amery, West, Shackleton, Totten), and the Antarctic Peninsula (George VI, Wilkins, Larsen C) show a statistically significant negative trend, which is largest for George VI (-4.6% decade^{-1}; Table 4). These trends are largely corroborated by the HIRHAM5 results. Two of the ice shelves (Fimbul and Baudouin) show (sometimes multiple) changepoints in their trends of MetUM MPI-freq (Fig. 5, Table 5). Based on MetUM, Fimbul (Baudouin) shows a decreasing trend of -4.6% decade^{-1} up to 1999 (-7.5% decade^{-1} up to 1998), followed by a weaker increasing trend of 2.2% decade^{-1} (4.3% decade^{-1}).

Figure 6 is analogous to Fig. 5 but showing the time series of MPI-int for a temperature/melt threshold of $T_0 = 273.15$ K. The trend lines are statistically insignificant for 10 of the 16 ice shelves (and there are also no changepoints). The

exception is Ronne–Filchner (MetUM only), Shackleton and Wilkins (HIRHAM5 only), and Getz, Pine Island, and George VI (both MetUM and HIRHAM5), which all show a significant decreasing trend, which is largest for Ronne–Filchner (-0.4 K decade^{-1}; Table 6). These ice shelves also all show a decreasing trend in MPI-freq (Fig. 5, Table 4). Interestingly, two ice shelves with some of the highest MPI values (George VI and Pine Island; Table 3) are characterized by significant negative trends in both MPI-freq and MPI-int (Tables 4 and 6). Additionally, Getz also has significant negative trends in both MPI-freq and MPI-int in both models, but its mean MPI-freq (MPI-int) is somewhat lower (substantially lower) than Pine Island.

d. Mechanisms responsible for interannual variability of melt potential

Next, we investigate large-scale atmospheric circulation features and possible connections to the tropics for interannual variability in MPI-freq for a temperature/melt threshold of $T_0 = 273.15$ K (using the OLR, SST, and ERA5 datasets). Figures 7 and 8 show detrended correlations of MetUM MPI-freq for eight West Antarctic ice shelves [ordered west (Ross) to east (Larsen C)]. Figure 7 shows tropical SST and OLR, and Southern Hemisphere streamfunction at 200 hPa (SF200)
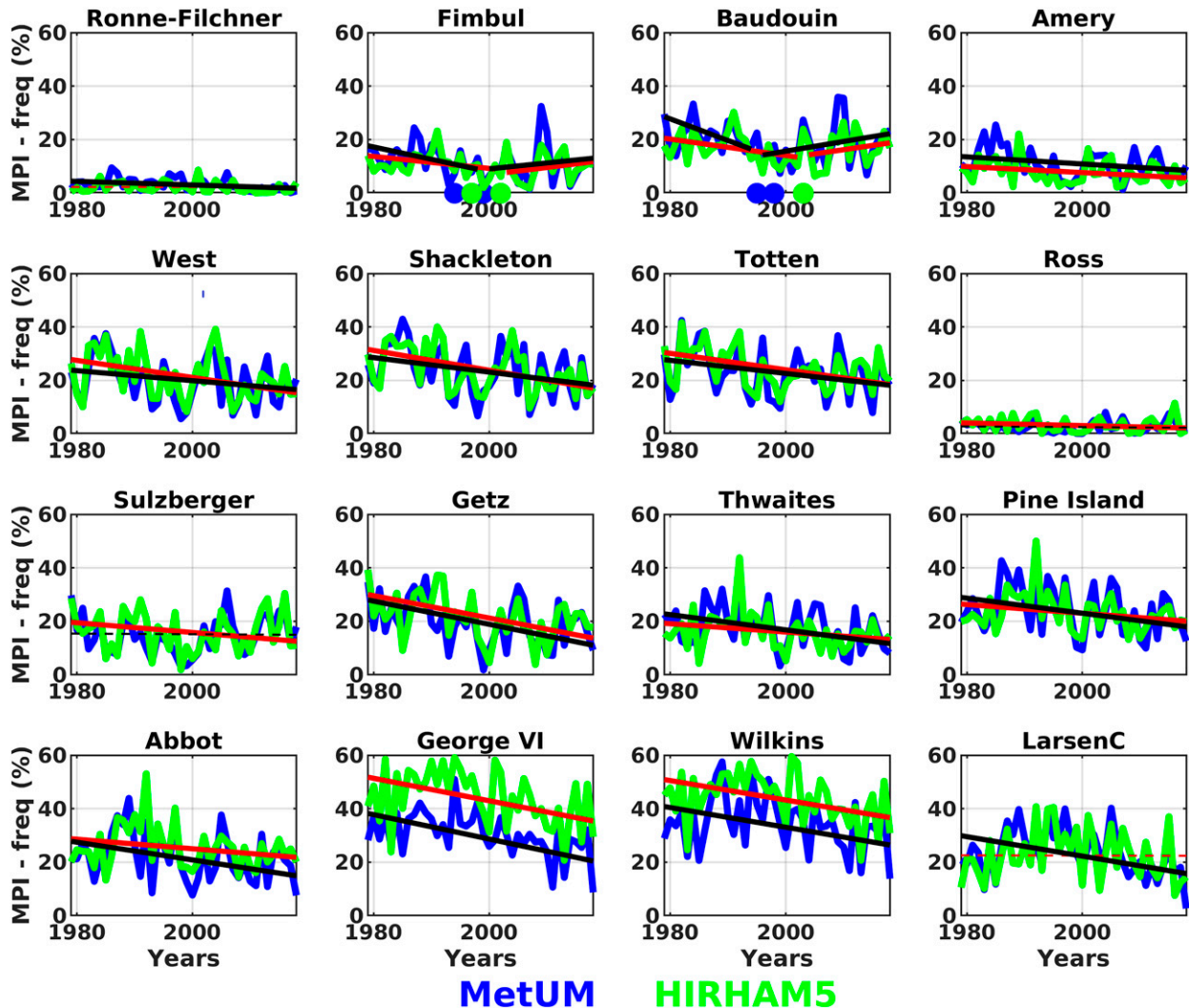
FIG. 5. Time series of MPI-freq for a temperature/melt threshold of $T_0 = 273.15$ K for the 16 Antarctic ice shelves examined based on MetUM (blue) and HIRHAM5 (green) output. The solid (dashed) lines show the statistically significant (insignificant) linear trends based on MetUM (black) and HIRHAM5 (red) output. The solid circle shows when a changepoint occurred based on MetUM (blue) and HIRHAM5 (green) simulations. For multiple changepoints, only the trendline corresponding to the steepest slope is shown. The ice shelves examined are (from top left to bottom right) Ronne–Filchner, Fimbul, Baudouin, Amery, West, Shackleton, Totten, Ross, Sulzberger, Getz, Thwaites, Pine Island, Abbot, George VI, Wilkins, and Larsen C.

and geopotential height at 500 hPa (Z500). Figure 8 shows regional Z500, MSLP, 2-m temperature, and 10-m meridional wind speed in order to identify the local circulation features associated with MPI-freq on West Antarctic ice shelves. Analogous correlations for seven East Antarctic ice shelves [ordered from west (Ronne–Filchner) to east (Totten)] are shown in Figs. 9 and 10. Qualitatively similar results are seen for MPI-int given that MPI-int and MPI-freq time series are positively correlated with values ranging from 0.72 (Larsen C) to 0.93 (Amery, Fimbul) based on MetUM and from 0.73 (Wilkins) to 0.93 (Amery) based on HIRHAM5 (Table 7). This also indicates that ice shelves with many melt-allowing days also have warmer melt-allowing days. Additionally, Table 8 (Table 9) shows that the detrended

correlations between MPI-freq (MPI-int) with SAM, Niño-4, and SOI indices are qualitatively similar based on both MetUM and HIRHAM5.

In West Antarctica, most ice shelves show a positive correlation with SST in the central tropical Pacific Ocean (strongest for Thwaites and Pine Island) along with a significant negative correlation with OLR (i.e., enhanced deep convection) extending southeastward along the South Pacific convergence zone (SPCZ). There are also significant positive OLR correlations (i.e., suppressed deep convection) over the Maritime Continent, and significant positive SST correlations in the tropical Indian Ocean/negative OLR correlations in eastern equatorial Africa (Fig. 7). In general, the SST and OLR correlations for West Antarctic ice shelves resemble an El Niño

TABLE 4. Linear trends in MPI-int (% yr^{-1}, second column) for the 16 ice shelves examined for a temperature/melt threshold of $T_0 = 273.15$ K. Results based on MetUM output are shown first and HIRHAM5 output second (i.e., MetUM, HIRHAM5). CP indicates the occurrence of a changepoint, which only occurred for MPI-freq for two ice shelves (Fimbul, Baudouin). Analogous results for the sensitivity test using a temperature/melt threshold value of $T_0^S = 271.15$ K (third column) with changepoints occurring for four ice shelves (Fimbul, Baudouin, Larsen C, Ross). Boldface trends are statistically significant at the 95% significance level.

Ice shelf	$T_0 = 273.15$ K (MetUM, HIRHAM5)	$T_0^S = 271.15$ K (MetUM, HIRHAM5)
Ronne–Filchner	**−0.07**, −0.00	**−0.24**, −0.01
Fimbul	CP, CP	CP, −0.09
Baudouin	CP, CP	CP, CP
Amery	**−0.13**, **−0.11**	**−0.31**, **−0.16**
West	**−0.19**, **−0.32**	**−0.21**, **−0.35**
Shackleton	**−0.27**, **−0.37**	**−0.23**, **−0.30**
Totten	**−0.25**, **−0.31**	**−0.28**, **−0.31**
Ross	−0.01, **−0.05**	CP, **−0.12**
Sulzberger	−0.01, **−0.18**	**0.02**, −0.23
Getz	**−0.43**, **−0.42**	**−0.40**, **−0.44**
Thwaites	**−0.29**, **−0.15**	**−0.38**, −0.12
Pine Island	**−0.28**, **−0.16**	**−0.30**, −0.05
Abbot	**−0.33**, **0.18**	**−0.37**, **0.11**
George VI	**−0.46**, **−0.42**	**−0.39**, **−0.23**
Wilkins	**−0.37**, **−0.36**	−0.11, **−0.13**
Larsen C	**−0.36**, −0.00	CP, **−0.12**

pattern, with the Amundsen Sea Embayment ice shelves (e.g., Getz, Thwaites, Pine Island, and Abbot) showing the strongest correlations with this tropical pattern, as well as being significantly correlated with either the oceanic (Niño-4) or atmospheric (SOI) component of ENSO (Table 8). However, the spatial pattern of the SST correlations in the Pacific resembles more of a central Pacific El Niño rather than a canonical eastern Pacific El Niño pattern (Ashok et al. 2007), and the strongest OLR correlations in the Pacific are oriented diagonally south of the Equator along the SPCZ. In fact, ice

shelves near and on the Antarctic Peninsula (Abbot, George VI, and Larsen C) generally have weak to near-zero correlations with equatorial Pacific SST and OLR anomalies and are significantly correlated with convection in the SPCZ only. Despite tropical teleconnections to southern high latitudes being generally weak in summer (Scott Yiu and Maycock 2019), recent studies have shown both ENSO and SPCZ variability can significantly influence West Antarctic surface air temperature and surface melt in summer (Nicolas et al. 2017; Deb et al. 2018; Clem et al. 2019, 2022; Johnson et al. 2022). In particular, the relationships found here are consistent with the El Niño influence on the strong summer surface melt event on the Ross ice shelf in January 2016 (Nicolas et al. 2017), and the SPCZ relationship with multidecadal summer climate variability across West Antarctica (Clem et al. 2019) and interannual variability in summer melt on Larsen C (Clem et al. 2022).

While the climatological atmospheric circulation across the extratropical Southern Hemisphere during summer is strongly zonally symmetric (Fogt et al. 2012) and the spatial pattern of the summertime ENSO teleconnection tends to manifest as a zonally symmetric circulation response through a zonal-mean transfer of transient eddy momentum (Karoly 1989; L'Heureux and Thompson 2006), the SF200 and Z500 correlations show West Antarctic MPI-freq is correlated with a strongly asymmetric pattern more characteristic of a Rossby wave (Fig. 7). All West Antarctic ice shelves are correlated with a strong regional anticyclonic anomaly in the high-latitude South Pacific centered to the northeast of the ice shelf. Ice shelves west of the Amundsen Sea Embayment (e.g., Ross and Sulzberger) are associated with a broad high pressure anomaly over the high-latitude South Pacific, while moving east toward the Amundsen Sea Embayment and Antarctic Peninsula the high pressure anomaly becomes more regionally distinct. For the latter, the broad circulation pattern shows a great-circle path emanating from the central tropical Pacific seen in both the upper-tropospheric streamfunction field (which shows a significant anticyclonic anomaly on the poleward edge of the

TABLE 5. Linear trends in MPI-freq (% yr^{-1}) before (fifth column) and after (sixth column) the occurrence of a changepoint (CP) for a particular ice shelf (first column) and at a particular year (fourth column) based on either MetUM or HIRHAM5 (third column) output. The first seven rows show results for a temperature/melt threshold of $T_0 = 273.15$ K. The final five rows show results for the sensitivity test using a temperature/melt threshold value of $T_0^S = 271.15$ K. Boldface trends are statistically significant at the 95% significance level.

| Ice Shelf	Threshold	Model	CP year	Trend before CP	Trend after CP
Fimbul	$T_0 = 273.15$ K	MetUM	1994	**−0.40**	**0.18**
Fimbul	$T_0 = 273.15$ K	MetUM	1999	**−0.46**	**0.22**
Fimbul	$T_0 = 273.15$ K	HIRHAM5	1997	**−0.15**	**0.18**
Fimbul	$T_0 = 273.15$ K	HIRHAM5	2002	**−0.22**	**0.27**
Baudouin	$T_0 = 273.15$ K	MetUM	1995	**−0.81**	**0.36**
Baudouin	$T_0 = 273.15$ K	MetUM	1998	**−0.75**	**0.43**
Baudouin	$T_0 = 273.15$ K	HIRHAM5	2003	**−0.31**	**0.32**
Fimbul	$T_0^S = 271.15$ K	MetUM	2001	**−0.21**	**0.36**
Baudouin	$T_0^S = 271.15$ K	MetUM	1999	**−0.64**	**0.59**
Baudouin	$T_0^S = 271.15$ K	HIRHAM5	1997	**−0.19**	**0.30**
Larsen C	$T_0^S = 271.15$ K	MetUM	1999	**0.11**	**−1.45**
Ross	$T_0^S = 271.15$ K	MetUM	1994	**−1.17**	**0.21**
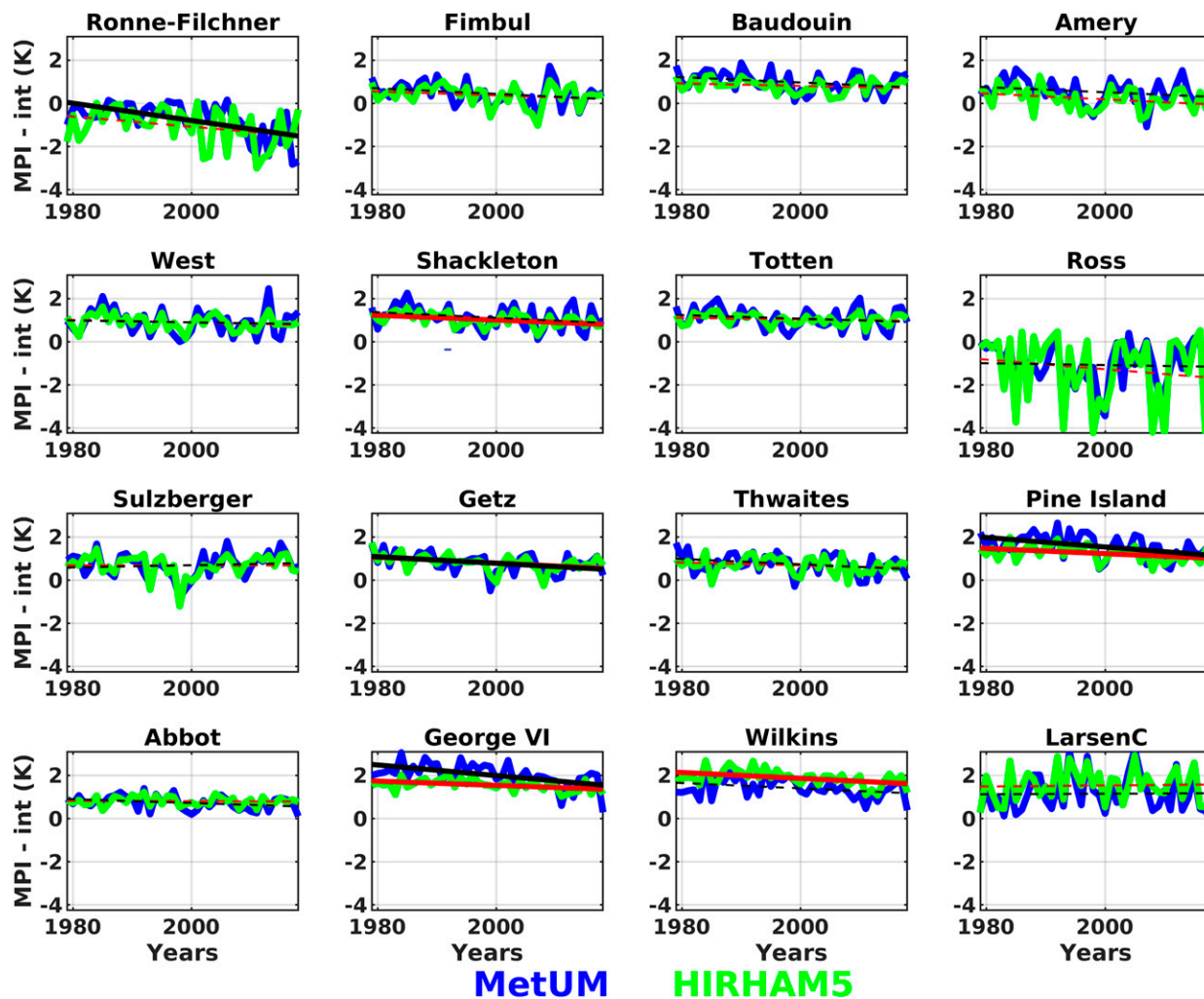
FIG. 6. As Fig. 5, but for MPI-int.

deep convection) and Z500 (which shows a great circle path stretching across the South Pacific from New Zealand into the South Atlantic). The zonally asymmetric pattern is further reflected in West Antarctic ice shelves showing no significant correlation with the SAM index (Table 8) as variability in the SAM would generally lead to zonally symmetric circulation anomalies.

Looking closer at the local circulation anomalies (Fig. 8), for all ice shelves the Z500 high pressure anomaly along the West Antarctic coast is flanked to the west by anomalously cyclonic flow, which would enhance the poleward advection of heat and moisture to the coast, and the pattern is equivalent barotropic stretching from 500 hPa down to the surface (i.e., MSLP). The 500-hPa ridge extends deeper into the West Antarctic interior, while the surface anticyclonic anomaly is located to the east of the ice shelve and just offshore of the coast. The correlations with 10-m meridional wind and 2-m temperature show that the circulation anomalies produce anomalous warm northerly flow on the western edge of the anticyclone/in the warm sector of the cyclone, indicating

the northerly advection of warm maritime air is key to producing high MPI-freq along coastal West Antarctica.

Turning to East Antarctica (Figs. 9 and 10), many ice shelves also show significant positive correlations with central tropical Pacific SSTs (Fig. 9), with several being significantly correlated with Niño-4 and SOI (Amery, West, Shackleton) (Table 8). Ronne–Filchner, technically located in West Antarctic but east of the Antarctic Peninsula, stands in stark contrast to the other East Antarctic ice shelves and generally shows a circulation pattern more consistent with the West Antarctic ice shelves, specifically a regional high pressure anomaly in the Weddell Sea flanked by low pressure to the west (Fig. 10). Together this leads to anomalous warm northerly flow from the Bellingshausen Sea across Ellsworth Land that descends onto the ice shelf from the interior, and warm northerly flow from the Weddell Sea (Fig. 10). The former is consistent with Scott et al. (2019) who found enhanced surface melt on Ronne–Filchner to be associated with warm advection from Ellsworth Land. Similarly, Ronne–Filchner is significantly correlated with central tropical Pacific OLR and zonally asymmetric circulation anomalies across

TABLE 6. As in Table 4, but showing linear trends in MPI-int ($K\ yr^{-1}$) for the 16 ice shelves examined for a temperature/melt threshold of $T_0 = 273.15$ K. Correlation values for MPI-int for the sensitivity test using a temperature/melt threshold value of $T_0^S = 271.15$ K are identical to those for $T_0 = 273.15$ K. Boldface trends are statistically significant at the 95% significance level.

Ice shelf	$T_0 = 273.15$ K (and $T_0^S = 271.15$ K) (MetUM, HIRHAM5)
Ronne–Filchner	**−0.040**, −0.024
Fimbul	−0.013, −0.0091
Baudouin	−0.012, −0.0056
Amery	−0.012, −0.013
West	−0.0042, −0.0059
Shackleton	−0.013, **−0.011**
Totten	−0.0083, −0.0036
Ross	−0.0042, −0.022
Sulzberger	0.0053, −0.000040
Getz	**−0.015, −0.014**
Thwaites	−0.012, −0.0067
Pine Island	**−0.022, −0.012**
Abbot	−0.0088, −0.0011
George VI	**−0.025, −0.0098**
Wilkins	−0.012, **−0.014**
Larsen C	0.0012, 0.0023

the Southern Hemisphere (Fig. 9) and no significant correlation with the SAM (Table 8).

In contrast, the atmospheric circulation associated with enhanced MPI-freq for East Antarctic ice shelves to the east of

Ronne–Filchner (e.g., Fimbul, Baudouin, Amery, West, Shackleton, Totten) rapidly transitions to a zonally symmetric pattern characteristic of the negative SAM phase, with strong positive Z500 (and MSLP) correlations over the Antarctic continent and a zonal band of negative Z500 (and MSLP) correlations across middle latitudes (Figs. 9 and 10). Indeed, MPI-freq for all East Antarctic ice shelves (from Fimbul to Totten) are significantly negatively correlated with the SAM index (Table 8). Embedded within the anomalous high pressure over the Antarctic interior, the SF200 correlations generally show locally enhanced anticyclonic circulation on the plateau to the east of each ice shelf which would locally enhance east to northeasterly flow along the coast (Fig. 9). The 10-m meridional wind and 2-m temperature correlations (Fig. 10) show MPI-freq is tied to anomalous northerly maritime flow for Fimbul and Baudouin, but this is not seen for the remaining East Antarctic ice shelves. And in contrast to West Antarctica, all the East Antarctic ice shelves are associated with widespread anomalous warm conditions over the East Antarctic interior characteristic of the negative SAM pattern rather than local meridional thermal advection (Fig. 10). The 2-m temperature anomalies are locally strongest along the coast near each respective ice shelf coinciding with enhanced (geostrophic) coastal easterlies. On the other hand, Amery shows a significant correlation with (southerly) flow descending off the plateau, which has previously been shown to lead to locally enhanced foehn warming of the maritime air by 5–7 K (Turner et al. 2021).
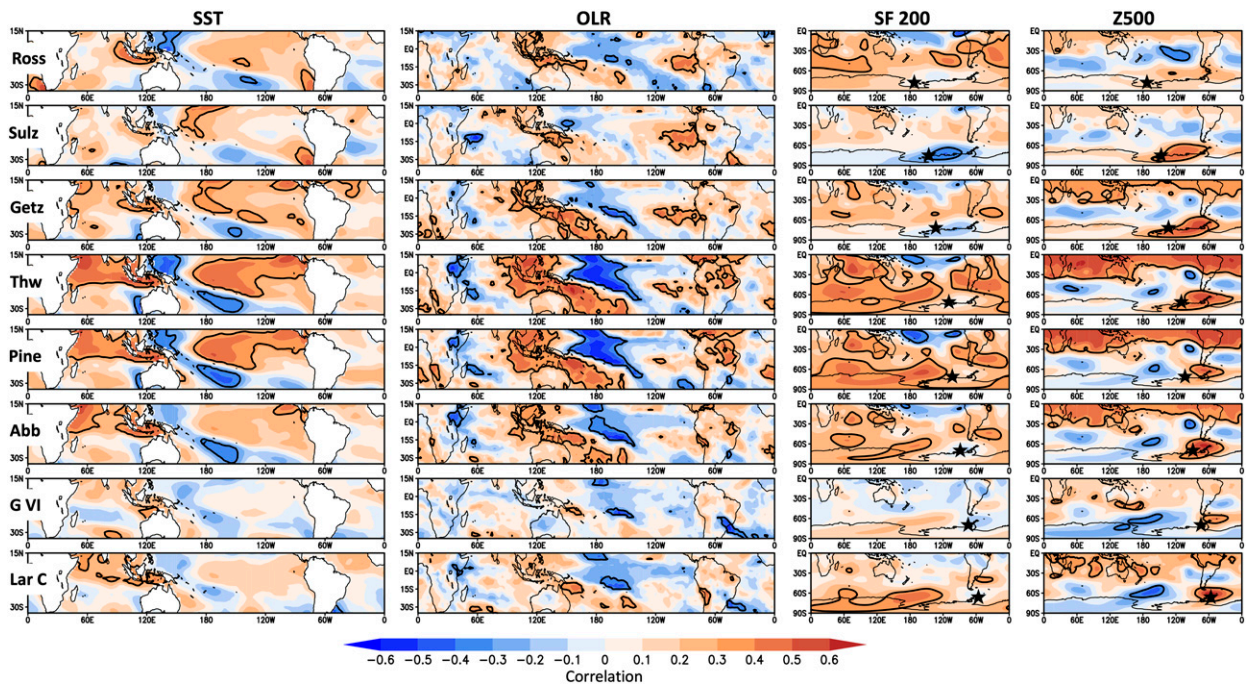

FIG. 7. Detrended correlation (shaded) between MPI-freq based on MetUM output for a temperature/melt threshold of $T_0 = 273.15$ K for West Antarctic ice shelves and tropical (30°S–15°N) (first column) sea surface temperature and (second column) outgoing longwave radiation, and Southern Hemisphere (90°–0°S) (third column) streamfunction at 200 hPa and (fourth column) geopotential height at 500 hPa. The ice shelves examined are (from top to bottom) Ross, Sulzberger, Getz, Thwaites, Pine Island, Abbot, George VI, and Larsen C. The location of each ice shelf examined is marked by a black star in the third and fourth columns. The bold black contour denotes statistically significant correlations at the 95% significance level.
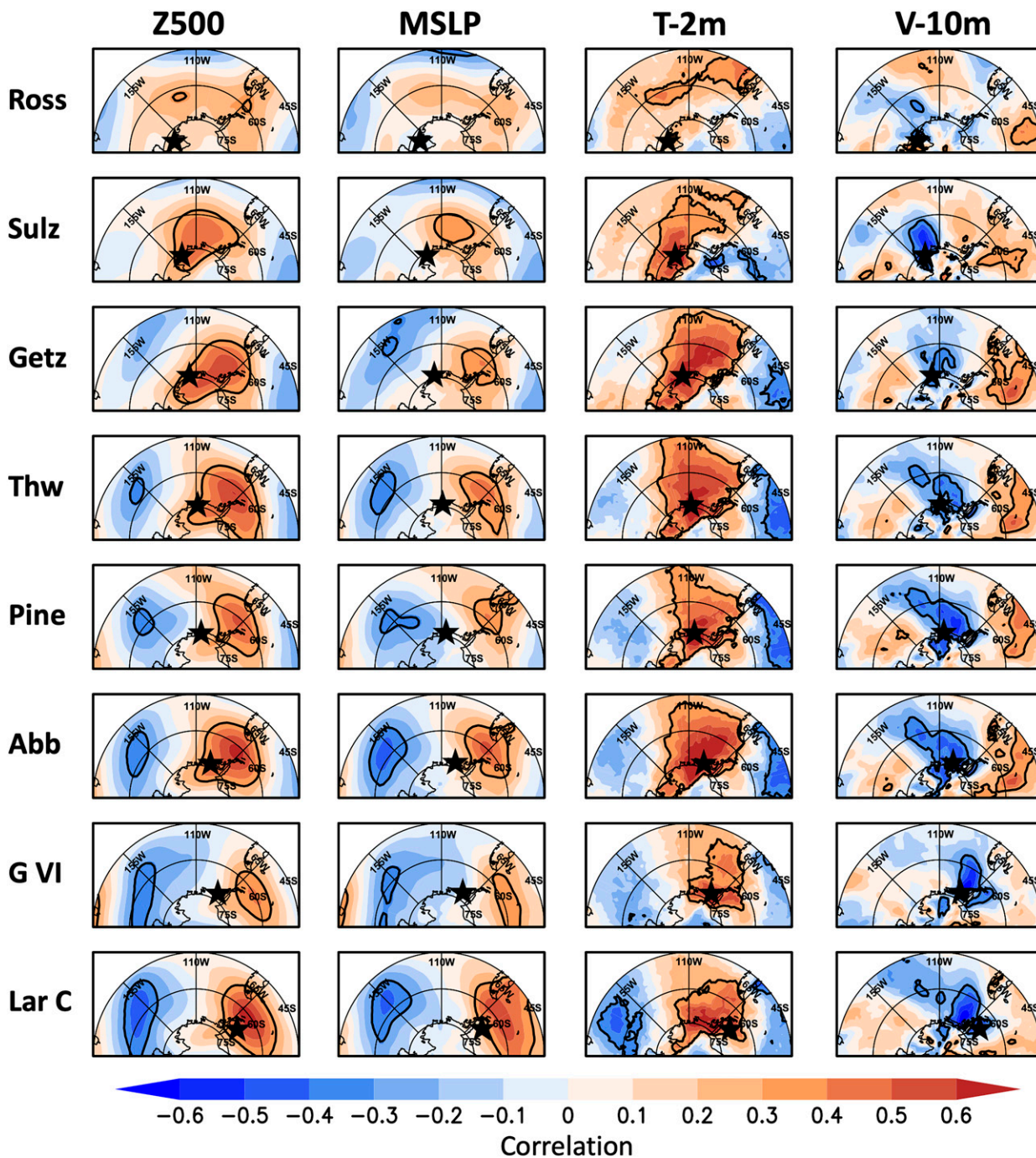
FIG. 8. As in Fig. 7, but zoomed in over West Antarctica and the surrounding Southern Ocean and showing results for (first column) geopotential height at 500 hPa, (second column) mean sea level pressure, (third column) 2-m temperature, and (fourth column) 10-m meridional wind speed. The location of each ice shelf examined is marked by a black star.

We further investigate the circulation patterns and their mechanisms with a composite analysis of the top six highest minus the top six lowest MPI-freq years (85th and 15th percentiles, respectively) (Fig. 11). To reduce the effects of outlier years tied to local mesoscale processes and better capture the large-scale patterns, the years selected for compositing were based on averaged standardized MPI-freq anomalies for three groups of ice shelves based on qualitatively similar local and large-scale circulation features. The groups chosen are 1) Fimbul and Baudoin (western East Antarctica) based on their stronger correlation with northerly maritime flow, 2) Amery, West, Shackleton, and Totten (eastern East Antarctica) based on
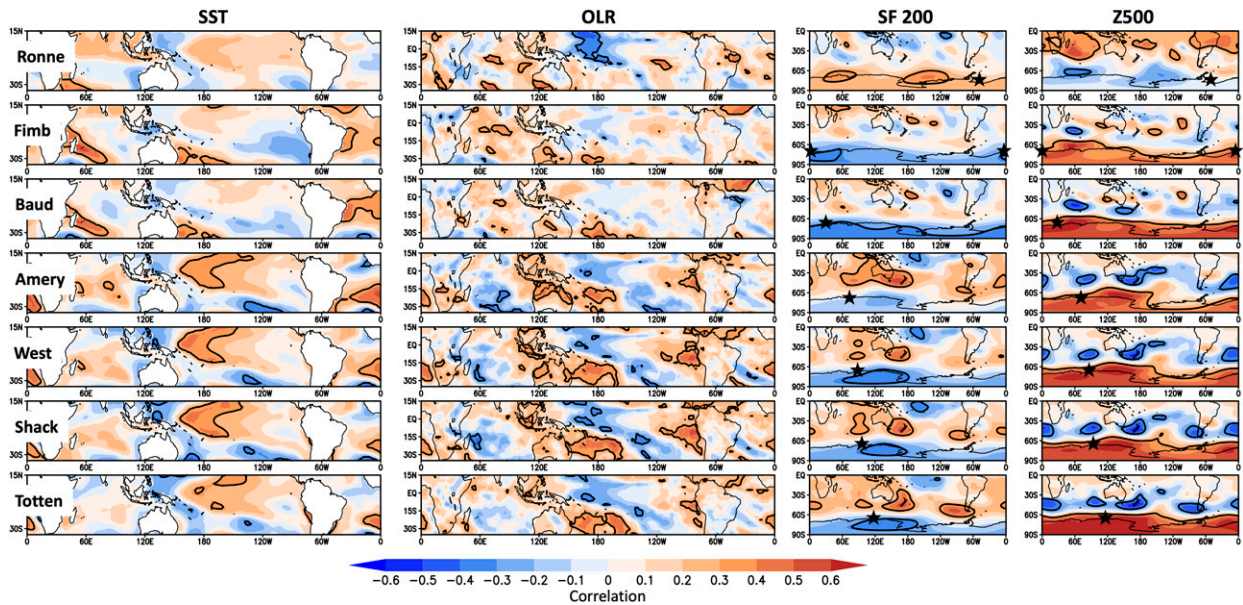
FIG. 9. As in Fig. 7, but showing results for East Antarctic ice shelves. The ice shelves examined are (from top to bottom) Ronne–Filchner, Fimbul, Baudouin, Amery, West, Shackleton, and Totten. The location of each ice shelf examined is marked by a black star.

their stronger correlation with easterly or offshore flow, and 3) Pine Island and Thwaites (West Antarctica) based on their strong correlations with tropical Pacific SST and OLR.

For West Antarctica (right column, Fig. 11), high versus low MPI-freq years show strong anomalous central tropical Pacific convection and reduced convection over the Maritime Continent, with no other significant OLR anomalies. This indicates that despite the broad correlations with OLR (and SST) across the tropics seen in Fig. 7, the central tropical Pacific convection is likely the key driver of the circulation anomalies and the other correlations are likely tied to the far-reaching influence of tropical Pacific convection across the tropics (e.g., Alexander et al. 2002). The SF200 and stationary wave flux clearly illustrate great circle stationary Rossby wave propagation from the subtropical southeast Pacific across the Antarctic Peninsula and into the South Atlantic. The Z500 shows a slightly eastward displaced El Niño–like Pacific–South America pattern stretching from east of New Zealand to the South Atlantic, resulting in a strong anticyclone over the Antarctic Peninsula region that causes strong local warm maritime northerly flow to the Amundsen Sea Embayment.

For East Antarctica (left and center columns, Fig. 11), the anomalies in tropical convection are weak and generally insignificant, and the atmospheric circulation anomalies are strongly zonally symmetric (high pressure over Antarctica, low pressure across middle latitudes) along with significant circumpolar easterly wind anomalies (weaker westerlies) across much of the Southern Ocean, both reflecting the negative phase of the SAM. Both East Antarctic regions show anomalous poleward wave propagation into the interior which appears to locally build high pressure on the plateau and locally enhances coastal easterly flow near each group of ice shelves. Importantly, the stationary wave propagation onto the plateau originates over

high latitudes within the core of the midlatitude storm track, with a less marked great circle path originating in tropical latitudes as seen in West Antarctica. This indicates the anticyclone over the plateau has likely become cut off from the mean midlatitude wave activity rather than a result of a tropically forced Rossby wave.

e. Sensitivity test using a temperature/melt threshold of $T_0^S = 271.15\,K$

Values of MPI for the sensitivity test using a temperature/melt threshold value of $T_0^S = 271.15\,\mathrm{K}$ are around 3–4 times larger for the 16 ice shelves compared to $T_0 = 273.15\,\mathrm{K}$ (Table 3). For example, MPI-freq (MPI-int) is around 70% (3–4 K) for Antarctic Peninsula ice shelves and 10% (1–2 K) for Ronne–Filchner and Ross, and typically between 40% and 60% ($\sim$3 K) for the other ice shelves using $T_0^S = 271.15\,\mathrm{K}$. MPI values for Pine Island are again noticeably higher compared to other West Antarctic ice shelves (49.5% and 3.7 K based on MetUM). Spatial patterns/hotspots of MPI for $T_0^S = 271.15\,\mathrm{K}$ (Fig. 12) are broadly similar to those for $T_0 = 273.15\,\mathrm{K}$ (Fig. 4), but with markedly higher values. This is consistent with the same combination of climatological influences like the Amundsen Sea low, as well as local scale processes associated with warm signatures (such as foehn events, katabatic winds, and barrier winds), determining these patterns. However, this analysis shows that MetUM MPI-freq for $T_0^S = 271.15\,\mathrm{K}$ approaches 100% over the northern section of Larsen C (i.e., each summer day this region experiences daily maximum temperatures above this threshold), while MPI-int reaches 5 K.

Table 4 shows linear trends in MPI-freq for $T_0^S = 271.15\,\mathrm{K}$, which are broadly similar to those for $T_0 = 273.15\,\mathrm{K}$. In the case of MPI-int the linear trends are exactly the same (Table 6),
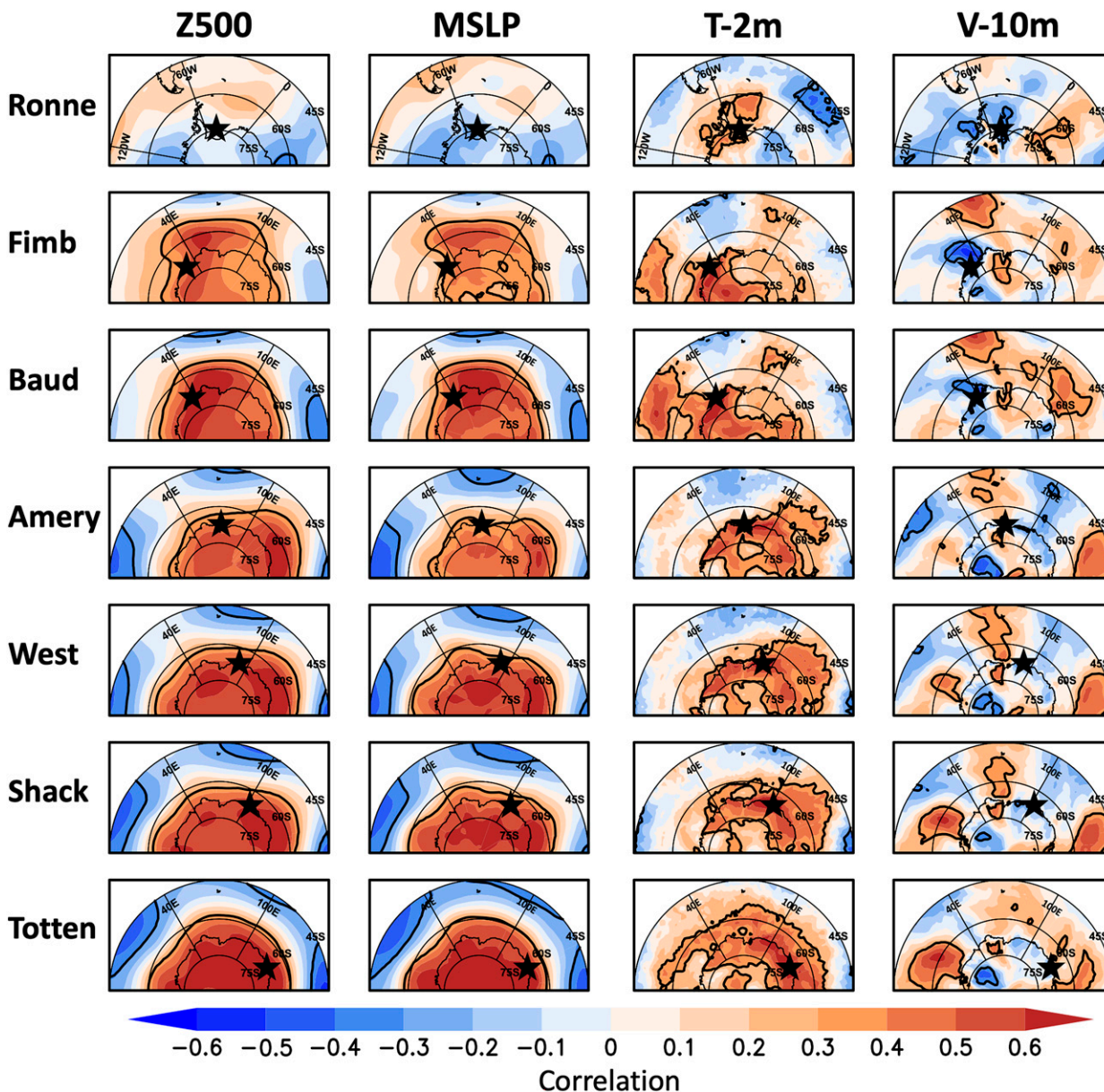
FIG. 10. As in Fig. 8, but showing results for East Antarctic ice shelves and zoomed in over East Antarctica and the surrounding Southern Ocean. The ice shelves examined are (from top to bottom) Ronne–Filchner, Fimbul, Baudouin, Amery, West, Shackleton, and Totten. The location of each ice shelf examined is marked by a black star.

as the time series for each threshold simply differs in magnitude by 2 K. However, it is noticeable that Larsen C and Ross now show a changepoint in the MPI-freq trend (Table 5; based on MetUM only). Larsen C shows an increasing trend of 1.1% decade^{-1} up to 1999, followed by a much stronger decreasing trend of -14.5% decade^{-1}, which is consistent with similar trends in temperature in response to changes in the interdecadal Pacific oscillation (Turner et al. 2016). Ross shows a decreasing trend of -11.7% decade^{-1} up to 1994, followed by a much weaker increasing trend of 2.1% decade^{-1}.

Table 7 shows that the correlation values between MPI-freq and MPI-int for $T_0^S = 271.15\,\mathrm{K}$, which although significant for each ice shelf are slightly lower (with the exception of Ross and Ronne–Filchner) for 271.15 K compared to $T_0 = 273.15$ K based on MetUM output. Detrended correlations between MPI-freq with SAM, Niño-4, and SOI indices based on a threshold of $T_0^S = 271.15\,\mathrm{K}$ for each ice shelf are qualitatively similar to values for $T_0 = 273.15$ K (Table 8). Note that for MPI-int, the correlations are not changed by adding a 2-K offset (Table 9). These results therefore confirm that the local and large-scale circulation patterns governing

TABLE 7. Correlation between the MPI-freq and MPI-int time series for the 16 ice shelves for a temperature/melt threshold of $T_0 = 273.15$ K (second column). Results based on MetUM output are shown first and HIRHAM5 output second (i.e., MetUM, HIRHAM5). Column three shows analogous results for the sensitivity test using a temperature/melt threshold value of $T_0^S = 271.15$ K. Boldface correlations are statistically significant at the 95% significance level.

Ice shelf	$T_0 = 273.15$ K (MetUM, HIRHAM5)	$T_0^S = 271.15$ K (MetUM, HIRHAM5)
Ronne–Filchner	**0.79, 0.81**	**0.85, 0.87**
Fimbul	**0.93, 0.92**	**0.78, 0.84**
Baudouin	**0.88, 0.87**	**0.67, 0.73**
Amery	**0.93, 0.93**	**0.80, 0.88**
West	**0.85, 0.86**	**0.57, 0.69**
Shackleton	**0.83, 0.85**	**0.71, 0.70**
Totten	**0.82, 0.77**	**0.62, 0.60**
Ross	**0.87, 0.82**	**0.93, 0.88**
Sulzberger	**0.87, 0.76**	**0.69, 0.64**
Getz	**0.88, 0.86**	**0.73, 0.70**
Thwaites	**0.78, 0.75**	**0.61, 0.58**
Pine Island	**0.77, 0.74**	**0.66, 0.49**
Abbot	**0.89, 0.76**	**0.79, 0.47**
George VI	**0.88, 0.77**	**0.68, 0.64**
Wilkins	**0.76, 0.73**	**0.49, 0.49**
Larsen C	**0.72, 0.86**	**0.53, 0.59**

MPI variability over West and East Antarctic ice shelves for a temperature threshold of $T_0^S = 271.15$ K are broadly similar to those for $T_0 = 273.15$ K, i.e., for West Antarctic ice shelves this resembles a tropically forced pattern, while East Antarctic ice shelves are more strongly tied to the negative SAM pattern, which can be amplified by El Niño conditions. These atmospheric patterns are also apparent from equivalent results

to Figs. 7–11 using the OLR, SST, and ERA5 datasets but for $T_0^S = 271.15$ K (not shown).

4. Discussion and conclusions

For this study, our aim is to provide an estimate of regional surface melt potential over Antarctic ice shelves using a temperature-based estimator/proxy of the intensity of melting, which we refer to as the melt potential index (MPI). This is characterized by two components measuring the frequency (MPI-freq) and intensity (MPI-int) of daily maximum temperatures exceeding a melt threshold of $T_0 = 273.15$ K, which are derived from high-resolution (12 km) MetUM and HIRHAM5 hindcasts. The advantage of using an index based on this model output is the comprehensive spatial coverage at high resolution and long time series (40 summer seasons), which enables extraction of meaningful statistics and characteristics for all Antarctic ice shelves. Additionally, investigation of results from two models enables model dependence and consistency to be assessed. Both models, and especially the MetUM, are able to adequately simulate actual daily maximum temperatures observed on or near to ice shelves despite being generally cold biased (Fig. 2, Table 2).

We identify that MPI-freq is highest for Antarctic Peninsula ice shelves (23%–35% of summer daily maximum temperatures exceed the melt threshold), lowest (2%–3%) for Ronne–Filchner and Ross, and typically between 10% and 24% for the other West and East Antarctic ice shelves (Fig. 3, Table 3). Values of MPI-int are also highest for Antarctic Peninsula ice shelves (1.2–2.2 K above the threshold), lowest for Ronne–Filchner and Ross (<0 K), and around 0.6–1.7 K for other West and East Antarctic ice shelves (Fig. 3, Table 3). The strong correlation between MPI-freq and MPI-int (Table 7)

TABLE 8. Detrended correlation between MPI-freq for a temperature/melt threshold of $T_0 = 273.15$ K and Niño-4 (second column), SOI (third column), and SAM (fourth column) indexes for the 16 ice shelves examined. In each column the correlation values based on MetUM output are shown first, followed by HIRHAM5. Columns five, six, and seven show analogous results for the sensitivity test using a temperature/melt threshold value of $T_0^S = 271.15$ K. Boldface correlations are statistically significant at the 95% significance level.

Ice shelf	$T_0 = 273.15$ K (MetUM, HIRHAM5) Niño-4	SOI	SAM	$T_0^S = 271.15$ K (MetUM, HIRHAM5) Niño-4	SOI	SAM
Ronne	0.24, −0.09	−0.11, 0.16	0.21, 0.18	0.21, −0.13	−0.13, 0.18	0.14, 0.10
Fimbul	0.12, 0.21	0.00, −0.17	**−0.36, −0.34**	0.12, 0.17	−0.04, −0.14	**−0.44, −0.42**
Baudouin	0.10, 0.15	−0.07, −0.24	**−0.57, −0.33**	0.17, 0.19	−0.25, −0.27	**−0.55, −0.18**
Amery	**0.33, 0.20**	**−0.35, −0.26**	**−0.47, −0.34**	**0.32, 0.20**	−0.29, −0.22	**−0.62, −0.36**
West	**0.31, 0.38**	**−0.31, −0.51**	**−0.58, −0.60**	**0.31, 0.41**	−0.27, **−0.48**	**−0.61, −0.54**
Shackleton	**0.35, 0.46**	**−0.35, −0.52**	**−0.58, −0.59**	**0.38, 0.40**	**−0.34, −0.45**	**−0.51, −0.54**
Totten	0.29, **0.34**	−0.30, **−0.46**	**−0.67, −0.66**	**0.37, 0.36**	**−0.39, −0.46**	**−0.57, −0.57**
Ross	0.25, 0.12	−0.29, −0.30	−0.11, **−0.35**	0.27, 0.18	−0.26, −0.28	−0.02, −0.27
Sulzberger	0.22, 0.14	−0.12, −0.26	−0.15, **−0.37**	0.26, 0.15	−0.07, −0.23	−0.17, **−0.36**
Getz	**0.31, 0.39**	−0.30, **−0.41**	−0.19, −0.25	**0.44, 0.40**	**−0.35, −0.40**	**−0.31, −0.13**
Thwaites	**0.45, 0.34**	**−0.41, −0.42**	−0.07, −0.07	**0.43, 0.41**	**−0.43, −0.51**	−0.10, −0.01
Pine	**0.44, 0.35**	**−0.43, −0.37**	0.04, 0.01	**0.34, 0.42**	**−0.39, −0.46**	0.06, 0.12
Abbot	0.25, **0.34**	**−0.33, −0.38**	0.00, −0.03	0.23, **0.46**	−0.27, **−0.48**	0.05, 0.19
George VI	0.00, **0.36**	−0.11, **−0.42**	0.22, 0.25	0.07, **0.37**	−0.19, **−0.37**	0.26, **0.45**
Wilkins	−0.01, 0.24	−0.12, −0.25	0.26, **0.35**	−0.12, 0.28	−0.02, −0.23	0.23, **0.61**
Larsen C	0.16, 0.04	−0.17, −0.04	0.15, **0.37**	0.00, 0.17	−0.11, **−0.32**	−0.01, 0.21

TABLE 9. Detrended correlation between MPI-int for a temperature/melt threshold of $T_0 = 273.15$ K and Niño-4 (second column), SOI (third column), and SAM (fourth column) indexes for the 16 ice shelves examined. In each column the correlation values based on MetUM output are shown first, followed by HIRHAM5. Correlation values for MPI-int for the sensitivity test using a temperature/melt threshold value of $T_0^S = 271.15$ K are identical to those for $T_0 = 273.15$ K. Boldface correlations are statistically significant at the 95% significance level.

Ice shelf	$T_0 = 273.15$ K (and $T_0^S = 271.15$ K) (MetUM, HIRHAM5)		
	Niño-4	SOI	SAM
Ronne	0.21, −0.13	−0.14, 0.15	0.14, 0.17
Fimbul	0.16, 0.25	−0.07, −0.24	**−0.45**, **−0.36**
Baudouin	0.05, 0.26	−0.04, −0.30	**−0.53**, **−0.37**
Amery	**0.41**, 0.28	**−0.40**, **−0.33**	**−0.41**, **−0.45**
West	0.19, **0.37**	−0.14, **−0.42**	**−0.42**, **−0.53**
Shackleton	0.21, **0.44**	−0.15, **−0.40**	**−0.48**, **−0.53**
Totten	0.18, 0.20	−0.12, −0.25	**−0.51**, **−0.50**
Ross	0.29, **0.35**	**−0.31**, **−0.39**	−0.09, −0.25
Sulzberger	0.21, 0.22	−0.12, −0.29	−0.16, **−0.36**
Getz	0.18, 0.28	−0.19, −0.26	−0.14, −0.20
Thwaites	0.24, 0.26	−0.14, −0.26	0.03, −0.02
Pine	**0.33**, 0.22	−0.20, −0.20	0.03, −0.07
Abbot	0.27, 0.26	−0.30, −0.19	−0.02, −0.09
George VI	−0.12, 0.24	0.02, −0.22	0.11, 0.14
Wilkins	−0.13, 0.00	0.06, −0.01	0.10, 0.17
Larsen C	0.07, 0.00	−0.19, −0.04	0.19, 0.28

indicates that ice shelves and years with many melt-allowing days also have warmer melt-allowing days. The high MPI values for Larsen C and Wilkins (Antarctic Peninsula) are particularly important as these regions are especially vulnerable to hydrofracture if inundated by surface meltwater, in contrast to some others that despite high MPI are located in regions that are more resilient to hydrofracture, such as George VI, Baudouin, and Amery (Lai et al. 2020). Our results further identify that Pine Island has an especially high MPI of 23.7% and 1.7 K (the highest outside of the Antarctic Peninsula), which suggests it is vulnerable to extreme surface melt events in addition to the well-known basal melting (Jenkins et al. 2010, 2016). Many ice shelves are characterized by pronounced spatial gradients in MPI, which we suggest is explained by warm signatures associated by local effects such as foehn winds, katabatic winds, barrier winds, and the Ross Ice Shelf air stream (Fig. 4). The ice shelves characterized by high MPI largely agree with those identified by Trusel et al. (2015), Feron et al. (2021), and Gilbert and Kittel (2021).

Ice shelves around Antarctica (with the exception of Ross and Sulzberger) show a significant negative trend in MPI-freq based on MetUM (Fig. 5, Table 4). Two of the ice shelves (Fimbul and Baudouin) show changepoints in their trends of MPI-freq (Fig. 5, Table 5), characterized by a decreasing trend up to the end of the twentieth century. By contrast, the only significant trends in MPI-int based on MetUM are negative for Ronne–Filchner, Getz, Pine Island and George VI (Fig. 6, Table 6). Interestingly, two ice shelves with some of

the highest MPI values (George VI and Pine Island; Table 3) are characterized by negative trends in both MPI-freq and MPI-int (as is Getz), suggesting that although they are clearly vulnerable to extreme surface melt events, widespread surface melting might be less common in recent decades.

We typically do not find these trends based on satellite passive microwave observations of melt (e.g., Scott et al. 2019; Johnson et al. 2022). For example, Johnson et al. (2022, their Fig. 4) found no significant linear trends in annual melt duration over the period 1979–2020 averaged over all pixels on each of the 30 Antarctic ice shelves they investigated, which is likely related to the high interannual variability in melt days that tends to characterize these ice shelves. However, Johnson et al. (2022) did find significant negative trends in melt duration for many individual pixels over Antarctic Peninsula ice shelves from 1995 to 2005, in agreement with Picard et al. (2007), and consistent with the MPI-freq trends in Fig. 5 and similar trends in temperature (Turner et al. 2016) in response to changes in the interdecadal Pacific oscillation.

The correlation (Figs. 7–10, Tables 8 and 9) and composite (Fig. 11) analysis reveal distinctly different local and large-scale circulation patterns governing MPI over West and East Antarctic ice shelves. In West Antarctica, local warm northerly advection of maritime air between a regional high pressure anomaly over the high-latitude South Pacific and a cyclone to the west appears to be the key mechanism leading to enhanced MPI, while a zonally symmetric pattern with strong high pressure anomalies over continental Antarctica and weakened circumpolar westerlies/local intensification of surface coastal easterlies appears to be the key feature enhancing MPI on East Antarctic ice shelves. The West Antarctic circulation shows a strong connection with central tropical Pacific/El Niño activity (Deb et al. 2018), including anomalous deep convection in the SPCZ, and the post-1999 negative interdecadal Pacific oscillation phase and increase in La Niñas (Purich et al. 2016) may explain the regional cooling and decreasing trend in summer MPI-freq for West Antarctic ice shelves. By contrast, the East Antarctic circulation is more strongly tied to the negative SAM pattern, consistent with Johnson et al. (2022), which again can be amplified (weakened) by El Niño (La Niña) conditions (Fogt et al. 2011). Therefore, the increase in La Niñas combined with predominantly positive SAM phases since 2000 (Clem et al. 2020) may explain the regional cooling and decreasing trend in summer MPI-freq for East Antarctic ice shelves. The correlation analysis for MPI-int with Niño-4, SOI, and SAM is broadly similar to that for MPI-freq (Tables 8 and 9). However, the correlation with ENSO is generally weaker for MPI-int compared to MPI-freq for West Antarctic ice shelves (e.g., the only significant correlation between MPI-int and Niño-4 is for Pine Island), which we attribute perhaps to MPI-int being more strongly influenced by local processes driving temperature extremes in this region.

It is also likely that for some ice shelves our estimates of MPI based on a temperature/melt threshold of $T_0 = 273.15$ K are conservative/underestimated, and more realistic estimates require using a lower temperature threshold, i.e., regions characterized by high MPI could experience even stronger
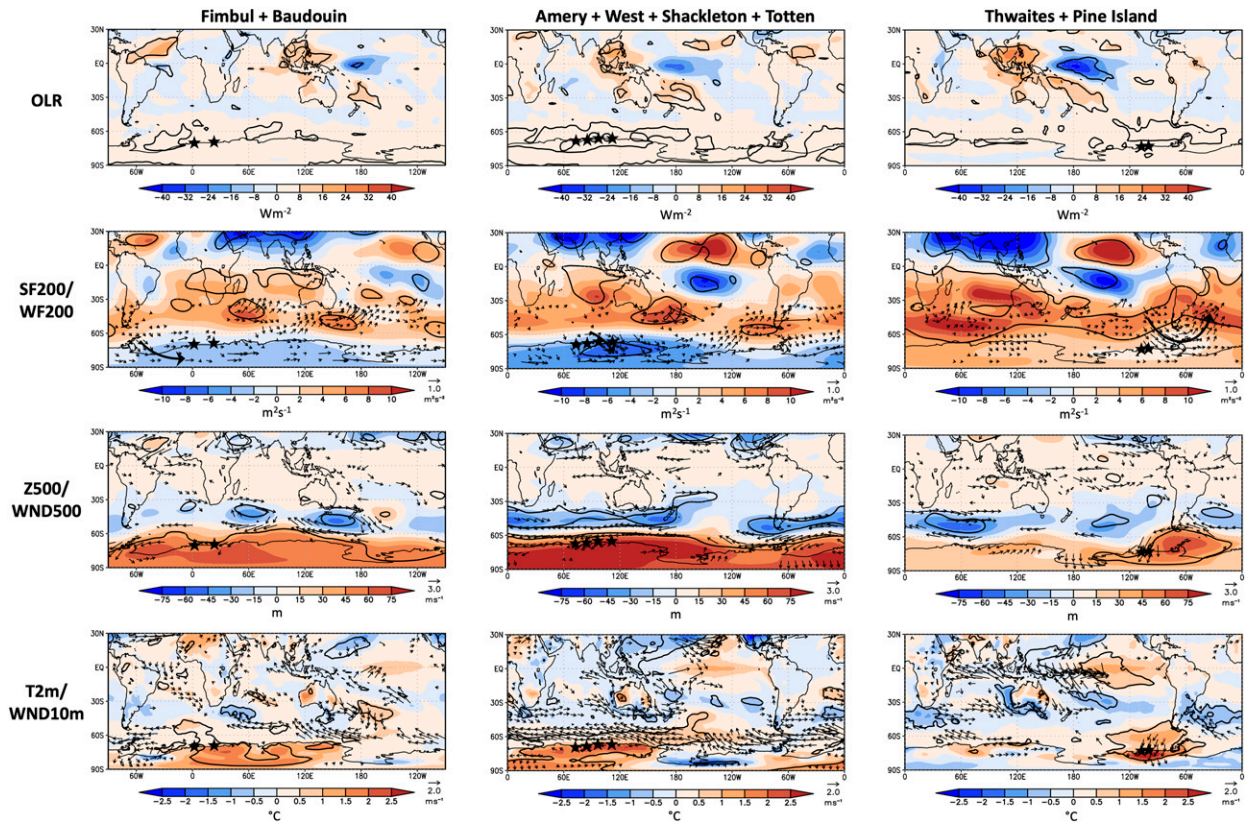
FIG. 11. Composite differences between averaged standardized high minus low MPI-freq years (top six minus bottom six, 85th/15th percentiles) based on MetUM output for a temperature/melt threshold of $T_0 = 273.15$ K of Southern Hemisphere and tropical (90°S–30°N) (first row) outgoing longwave radiation, (second row) streamfunction and horizontal wave flux at 200 hPa (shading and arrows, respectively), (third row) geopotential height and horizontal wind at 500 hPa (shading and arrows, respectively), and (fourth row) 2-m temperature and 10-m wind (shading and arrows, respectively) for (left) Fimbul and Baudoin (reflecting western East Antarctic ice shelves), (center) Amery, West, Shackleton, and Totten (reflecting central/eastern East Antarctic ice shelves), and (right) Pine Island and Thwaites (reflecting West Antarctic ice shelves). The bold black contour denotes differences that are significant at the 95% significance level; only vectors with at least one wind component significant at the 95% significance level are shown in the bottom two rows (wind at 500 hPa and at 10 m). The respective ice shelves are marked by black stars, and the local stationary Rossby wave propagation at 200 hPa is schematically drawn with a black arrow.

surface melting than our results suggest. This is for two reasons, first that melting can occur for temperatures lower than 273.15 K (e.g., Liston and Winther 2005; Tedesco 2009; Nicolas et al. 2017), and second because the MetUM and HIRHAM5 models have a cold summer daily maximum temperature bias (Fig. 2, Table 2). We investigated this in a sensitivity experiment by examining results for $T_0^S = 271.15$ K. Using this lower temperature threshold, we find that the MPI is around 3–4 times larger for the 16 ice shelves compared to $T_0 = 273.15$ K (Table 3, Fig. 12). For example, MPI-freq (MPI-int) is around 70% (3–4 K) for Antarctic Peninsula ice shelves and 10% (1–2 K) for Ronne–Filchner and Ross, and typically between 40% and 60% (~3 K) for the other ice shelves. Our results also show that the local and large-scale circulation patterns governing MPI variability over West and East Antarctic ice shelves for a temperature threshold of $T_0^S = 271.15$ K are broadly similar to those for $T_0 = 273.15$ K.

Our results show that MPI over West Antarctic ice shelves (with the exception of Sulzberger) is not significantly correlated

with the polarity of the SAM for a temperature threshold of $T_0 = 273.15$ K (Tables 8 and 9). This contrasts with recent results from studies based on satellite passive microwave observations of surface melting, which show that melting over West Antarctic ice shelves is significantly negatively correlated with the SAM (Scott et al. 2019; Johnson et al. 2022), perhaps because these tend to amplify the El Niño pattern (Fogt et al. 2011). However, the lack of correlation between the MPI index for West Antarctic ice shelves and the SAM found here is consistent with Deb et al. (2018, their Fig. 3). This study showed that the SAM does influence 2-m temperatures over ice shelves in this region simulated using the Polar Weather Research and Forecasting (Polar WRF) Model, but only below the melt threshold of 273.15 K. As our MPI uses a threshold of $T_0 = 273.15$ K, this therefore may help explain why our results did not find a significant correlation with the SAM index. Furthermore, the satellite-based time series of surface melt used by Scott et al. (2019) and Johnson et al. (2022) are able to identify the occurrence of liquid water at air temperatures lower that 273.15 K due
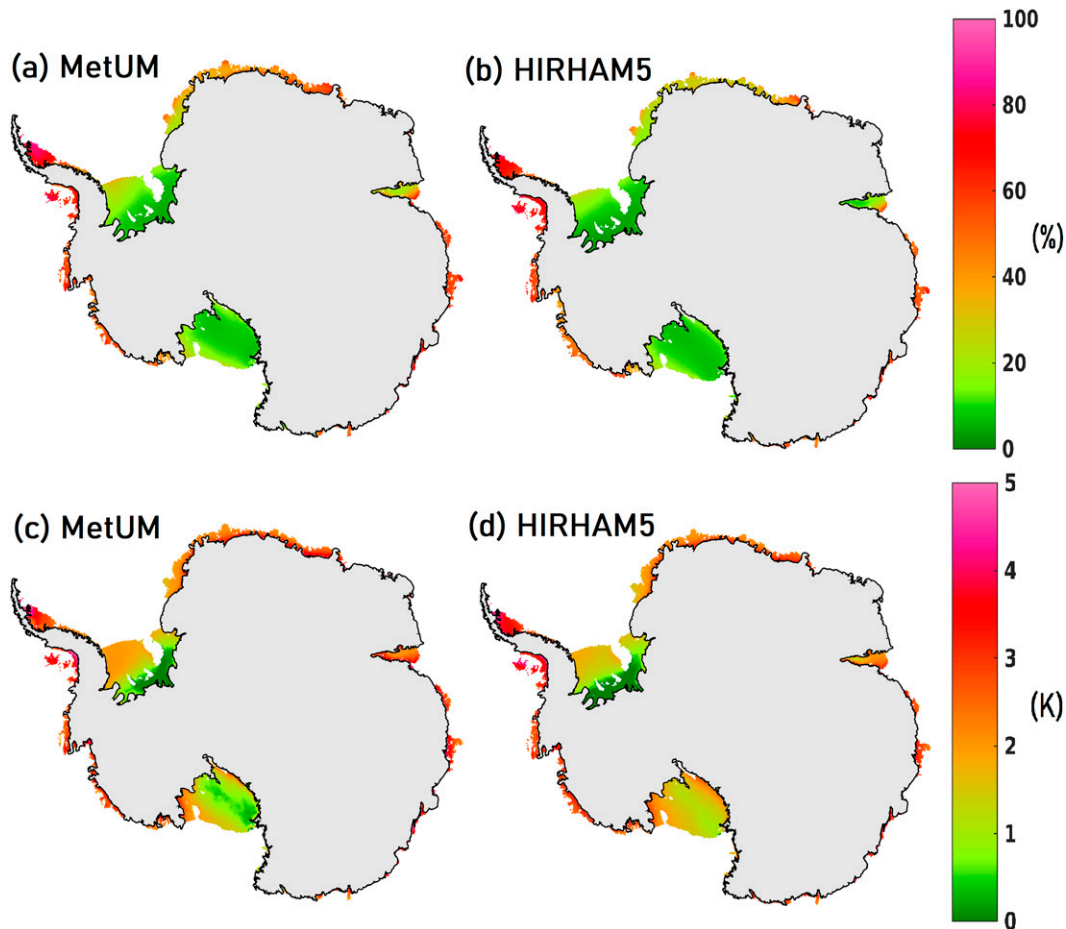
FIG. 12. As in Fig. 4, but for the sensitivity test using a temperature/melt threshold value of $T_0^S = 271.15$ K Note that this figure is not directly comparable with Fig. 4 because the range of the color bars is different.

to solar radiation (Tedesco 2009), and it is perhaps noteworthy that for the sensitivity test using a temperature/melt threshold value of $T_0^S = 271.15$ K that there is a negative significant relationship between MPI-freq and the SAM for Getz (-0.31, based on MetUM; Table 8) and Sulzberger (-0.36, based on HIRHAM5; Table 8), i.e., the SAM does influence summertime temperature extremes in this region but only below 273.15 K. For East Antarctic ice shelves our findings are broadly consistent with results by Johnson et al. (2022) showing that satellite observations of melting are significantly correlated with negative SAM.

We note that a limitation of this study is that the interpretation of the MPI-int results essentially assumes a linear relationship between its magnitude and the intensity of melting, when actually this relationship is nonlinear due to key aspects such as the melt–albedo feedback (Jakobs et al. 2021). The widely used positive-degree-day method also assumes an (empirical) linear relationship between air temperature and melt rates (Ohmura 2001; Hock 2005; van den Broeke et al. 2010). However, Jakobs et al. (2021) shows that for ice shelves in Antarctica with limited and infrequent melt (low MPI-freq), the relation between melt-allowing conditions and the actual season integrated amount of melt and melt days is poor, i.e.,

the melt–albedo feedback is strong. By contrast, for ice shelves with more frequent melt (high MPI-freq) there is a more consistent relationship between the frequency of melt-allowing days and season integrated melt intensity, i.e., the melt–albedo feedback is weak. Thus, we argue that our MPI metric is particularly suitable/justified for ice shelves characterized by higher (>200 mm w.e. yr^{-1}) melt rates required for ice shelf hydrofracturing due to these having a more linear relationship between surface melt and air temperature, and a useful metric in any case because of its simplicity and the robust capability of atmospheric models to simulate near-surface temperatures (Mottram et al. 2021; Carter et al. 2022). An alternative approach would have been to use the actual estimate of surface melting computed by the atmospheric models. However, the ability/sophistication of land surface snow schemes in models to capture this, as well as aspects such as the melt–albedo feedback, differs considerably in quality over Antarctica (Carter et al. 2022) and so makes intermodel and regional comparison difficult. For example, the setup of the MetUM in this study uses a so-called "zero-layer" snow scheme, which has shortcomings realistically representing surface melt because it 1) uses a composite snow/soil layer to simulate the thermal store of snow

and does not include any information on snowpack processes, and 2) the heat flux used to melt the surface is calculated as the residual in the surface energy budget whenever the surface temperature exceeds 0°C, after which it is reset to 0°C (Best et al. 2011). Hence our rationale for developing a relatively simple and robust temperature-based index as a proxy for melt production was to maximize the strength of the MetUM and its representation of its atmospheric components, rather than relying on simulated surface melt, which has known limitations. Comparing different outputs of simulated surface melt across various models (and explaining their differences and potential biases) is an important research need that is outside the scope of this study.

A further limitation is also that the model grid spacing of ~12 km is likely insufficient to accurately represent some of the local dynamical and physical processes that are associated with warm signatures/extreme temperature increases. For example, many modeling studies suggest that a grid spacing of 4 km or finer is necessary to realistically simulate foehn winds and their associated surface melting with reasonable accuracy (Kuipers-Munneke et al. 2018; Orr et al. 2021; Zou et al. 2021; Gilbert et al. 2022). Further, Orr et al. (2014) showed that the simulation of barrier winds using the MetUM was sensitive to grid spacing ranging from 12 to 1.5 km. Accurately representing small-scale resolution-dependent orographic features (such as hills, mountains, and cliffs) is also important as they can result in local variability in wind, temperature, and surface melt patterns (Orr et al. 2014; Alexander et al. 2017; Lenaerts et al. 2018). It would therefore be useful to do an additional sensitivity test using a higher grid spacing such as 4 km and investigate how the results change. Nevertheless, we note that despite the 12-km grid spacing that the MetUM MPI values showed a foehn signature for Larsen C and Ross (Figs. 4 and 12). However, differences between the MetUM and HIRHAM5 results, and more generally the cold bias exhibited by both models (Fig. 2, Table 2) is likely due to the treatment of 1) cloud microphysics, which has been shown to be important for realistically simulating surface melt over Antarctic ice shelves (King et al. 2015; Datta et al. 2019; Gilbert et al. 2020), 2) atmospheric boundary layer and turbulent fluxes, especially the development/breakdown of surface-based cold-air pools and associated temperature inversions (Seefeldt and Cassano 2008; Orr et al. 2021), and 3) surface and subsurface processes, which can impact near-surface temperatures (Walters et al. 2019).

Climate model experiments suggest a higher frequency of positive SAM conditions by the end of the twenty-first century due to global warming (Zheng et al. 2013), as well as a potential shift toward stronger and more frequent El Niño activity (Power et al. 2013; Santoso et al. 2013; Cai et al. 2014). Our study therefore suggests that these conditions may decrease (increase) the occurrence of favorable atmospherically driven surface melt over East (West) Antarctic ice shelves in the future. However, a rise in the mean temperature may lead to increased occurrences of temperatures above the melt threshold, and Feron et al. (2021) suggests that even under a moderate-emission greenhouse gas scenario (RCP4.5) the number of "very warm" summer days (i.e., days when the maximum temperature exceeds the 90th percentile threshold) will triple over East Antarctic ice shelves by the end of the twenty-first century. This suggests that although a trend toward more positive SAM conditions might suppress average circulation-driver melt over East Antarctic ice shelves, this may be counterbalanced by more frequent extreme events like heatwaves and atmospheric rivers that are associated with a disproportionate amount of total melting (Wille et al. 2019, 2021). Meanwhile, the suggested increase in intensification of surface melting over West Antarctic ice shelves, with an increase in atmospheric circulation patterns that favor enhanced surface melt working in tandem with increasing global temperatures, is consistent with other studies (Trusel et al. 2015; Feron et al. 2021; Gilbert and Kittel 2021), and in turn could potentially trigger further destabilization/retreat of the West Antarctic ice sheet (DeConto et al. 2021).

REFERENCES

Abel, S. J., and Coauthors, 2017: The role of precipitation in controlling the transition from stratocumulus to cumulus clouds in a Northern Hemisphere cold-air outbreak. *J. Atmos. Sci.*, **74**, 2293–2314, https://doi.org/10.1175/JAS-D-16-0362.1.

Abram, N. J., and Coauthors, 2013: Acceleration of snow melt in an Antarctic Peninsula ice core during the twentieth century. *Nat. Geosci.*, **6**, 404–411, https://doi.org/10.1038/ngeo1787.

Alexander, M. A., I. Bladé, M. Newman, J. R. Lanzante, N.-C. Lau, and J. D. Scott, 2002: The atmospheric bridge: The influence of ENSO teleconnections on air–sea interaction over the global oceans. *J. Climate*, **15**, 2205–2231, https://doi.org/10.1175/1520-0442(2002)015<2205:TABTIO>2.0.CO;2.

Alexander, S. P., A. Orr, S. Webster, and D. J. Murphy, 2017: Observations and fine-scale model simulations of gravity waves over Davis, East Antarctica (69°S, 78°E). *J. Geophys. Res. Atmos.*, **122**, 7355–7370, https://doi.org/10.1002/2017JD026615.

Arthur, J. F., C. Stokes, S. S. Jamieson, J. R. Carr, and A. A. Leeson, 2020: Recent understanding of Antarctic supraglacial lakes using satellite remote sensing. *Prog. Phys. Geogr. Earth Environ.*, **44**, 837–869, https://doi.org/10.1177/0309133320916114.

Ashok, K., S. K. Behera, S. A. Rao, H. Weng, and T. Yamagata, 2007: El Niño Modoki and its possible teleconnection. *J. Geophys. Res.*, **112**, C11007, https://doi.org/10.1029/2006JC003798.

Banwell, A. F., and D. R. MacAyeal, 2015: Ice-shelf fracture due to viscoelastic flexure stress induced by fill/drain cycles of supraglacial lakes. *Antarct. Sci.*, **27**, 587–597, https://doi.org/10.1017/S0954102015000292.

——, ——, and O. V. Sergienko, 2013: Breakup of the Larsen B Ice Shelf triggered by chain reaction drainage of supraglacial lakes. *Geophys. Res. Lett.*, **40**, 5872–5876, https://doi.org/10.1002/2013GL057694.

——, I. C. Willis, G. J. Macdonald, B. Goodsell, and D. R. MacAyeal, 2019: Direct measurements of ice-shelf flexure caused by surface melt-water ponding and drainage. *Nat. Commun.*, **10**, 730, https://doi.org/10.1038/s41467-019-08522-5.

——, R. T. Datta, R. L. Dell, M. Moussavi, L. Brucker, G. Picard, C. A. Shuman, and L. A. Stevens, 2021: The 32-year record-high surface melt in 2019/2020 on the northern George VI Ice Shelf, Antarctic Peninsula. *Cryosphere*, **15**, 909–925, https://doi.org/10.5194/tc-15-909-2021.

Barrand, N. E., D. G. Vaughan, N. Steiner, M. Tedesco, P. Kuipers Munneke, M. R. van den Broeke, and J. S. Hosking, 2013: Trends in Antarctic Peninsula surface melting conditions from observations and regional climate modeling. *J. Geophys. Res. Earth Surf.*, **118**, 315–330, https://doi.org/10.1029/2012JF002559.

Best, M. J., and Coauthors, 2011: The joint UK Land Environment Simulator (JULES), model description–Part 1: Energy and water fluxes. *Geosci. Model Dev.*, **4**, 677–699, https://doi.org/10.5194/gmd-4-677-2011.

Bozkurt, D., R. Rondanelli, J. C. Marin, and R. Garreaud, 2018: Foehn event triggered by an atmospheric river underlies record-setting temperature along continental Antarctica. *J. Geophys. Res. Atmos.*, **123**, 3871–3892, https://doi.org/10.1002/2017JD027796.

——, D. H. Bromwich, J. Carrasco, and R. Rondanelli, 2021: Temperature and precipitation projections for the Antarctic Peninsula over the next two decades: Contrasting global and regional climate model simulations. *Climate Dyn.*, **56**, 3853–3874, https://doi.org/10.1007/s00382-021-05667-2.

Bromwich, D. H., J. F. Carrasco, and C. R. Stearns, 1992: Satellite observations of katabatic-wind propagation for great distances across the Ross Ice Shelf. *Mon. Wea. Rev.*, **120**, 1940–1949, https://doi.org/10.1175/1520-0493(1992)120<1940:SOOKWP>2.0.CO;2.

Cai, W., and Coauthors, 2014: Increasing frequency of extreme El Niño events due to greenhouse warming. *Nat. Climate Change*, **4**, 111–116, https://doi.org/10.1038/nclimate2100.

Carter, J., A. Leeson, A. Orr, C. Kittel, and J. Melchior van Wessem, 2022: Variability in Antarctic surface climatology across regional climate models and reanalysis datasets. *Cryosphere*, **16**, 3815–3841, https://doi.org/10.5194/tc-16-3815-2022.

Christensen, O. B., M. Drews, J. H. Christensen, K. Dethloff, K. Ketelsen, I. Hebestadt, and A. Rinke, 2007: The HIRHAM regional climate model, version 5 (beta). DMI Tech. Rep. 06-17, 23 pp., https://backend.orbit.dtu.dk/ws/portalfiles/portal/51950450/HIRHAM.pdf.

Chyhareva, A., S. Krakovska, and D. Pishniak, 2019: Climate projections over the Antarctic Peninsula region to the end of the 21st century. Part I: Cold temperature indices. *Ukr. Antarct. J.*, **1**, 62–74, https://doi.org/10.33275/1727-7485.1(18).2019.131.

Clem, K. R., A. Orr, and J. O. Pope, 2018: The springtime influence of natural tropical Pacific variability on the surface climate of the Ross Ice Shelf, West Antarctica: Implications for ice shelf thinning. *Sci. Rep.*, **8**, 11983, https://doi.org/10.1038/s41598-018-30496-5.

——, B. R. Lintner, A. J. Broccoli, and J. R. Miller, 2019: Role of the South Pacific convergence zone in West Antarctic decadal climate variability. *Geophys. Res. Lett.*, **46**, 6900–6909, https://doi.org/10.1029/2019GL082108.

——, R. L. Fogt, J. Turner, B. R. Linter, G. J. Marshall, J. R. Miller, and J. A. Renwick, 2020: Record warming at the South Pole during the past three decades. *Nat. Climate Change*, **10**, 762–770, https://doi.org/10.1038/s41558-020-0815-z.

——, D. Bozkurt, D. Kennett, J. C. King, and J. Turner, 2022: Central tropical Pacific convection drives extreme high temperatures and surface melt on the Larsen C Ice Shelf, Antarctic Peninsula. *Nat. Commun.*, **13**, 3906, https://doi.org/10.1038/s41467-022-31119-4.

Coggins, J. H. J., A. J. McDonald, and B. Jolly, 2014: Synoptic climatology of the Ross Ice Shelf and Ross Sea region of Antarctica: *k*-mean clustering and validation. *Int. J. Climatol.*, **34**, 2330–2348, https://doi.org/10.1002/joc.3842.

Costanza, C. A., M. A. Lazzara, L. M. Keller, and J. J. Cassano, 2016: The surface climatology of the Ross Ice Shelf Antarctica. *Int. J. Climatol.*, **36**, 4929–4941, https://doi.org/10.1002/joc.4681.

Datta, R. T., M. Tedesco, X. Fettweis, C. Agosta, S. Lhermitte, J. T. M. Lenaerts, and N. Wever, 2019: The effect of Foehn-induced surface melt on firn evolution over the northeast Antarctic Peninsula. *Geophys. Res. Lett.*, **46**, 3822–3831, https://doi.org/10.1029/2018GL080845.

Deb, P., A. Orr, J. S. Hosking, T. Phillips, J. Turner, D. Bannister, J. O. Pope, and S. Colwell, 2016: An assessment of the Polar Weather Research and Forecasting (WRF) Model representation of near-surface meteorological variables over West Antarctica. *J. Geophys. Res. Atmos.*, **121**, 1532–1548, https://doi.org/10.1002/2015JD024037.

——, ——, D. H. Bromwich, J. P. Nicolas, J. Turner, and J. S. Hosking, 2018: Summer drivers of atmospheric variability affecting ice shelf thinning in the Amundsen Sea Embayment, West Antarctica. *Geophys. Res. Lett.*, **45**, 4124–4133, https://doi.org/10.1029/2018GL077092.

DeConto, R. M., and Coauthors, 2021: The Paris Climate Agreement and future sea-level rise from Antarctica. *Nature*, **593**, 83–89, https://doi.org/10.1038/s41586-021-03427-0.

Dee, D. P., and Coauthors, 2011: The ERA-Interim reanalysis: Configuration and performance of the data assimilation system. *Quart. J. Roy. Meteor. Soc.*, **137**, 553–597, https://doi.org/10.1002/qj.828.

Dell, R., N. Arnold, I. Willis, A. Banwell, A. Williamson, H. Pritchard, and A. Orr, 2020: Lateral meltwater transfer across an Antarctic Ice Shelf. *Cryosphere*, **14**, 2313–2330, https://doi.org/10.5194/tc-14-2313-2020.

Djoumna, G., and D. M. Holland, 2021: Atmospheric rivers, warm air intrusions, and surface radiation balance in the Amundsen Sea Embayment. *J. Geophys. Res. Atmos.*, **126**, e2020JD034119, https://doi.org/10.1029/2020JD034119.

Doake, C. S. M., H. F. J. Corr, H. Rott, P. Skvarca, and N. W. Young, 1998: Breakup and conditions for stability of the northern Larsen Ice Shelf, Antarctica. *Nature*, **391**, 778–780, https://doi.org/10.1038/35832.

Elvidge, A. D., I. A. Renfrew, J. C. King, A. Orr, and T. A. Lachlan-Cope, 2016: Foehn warming distributions in nonlinear and linear flow regimes: A focus on the Antarctic Peninsula. *Quart. J. Roy. Meteor. Soc.*, **142**, 618–631, https://doi.org/10.1002/qj.2489.

Feron, S., R. R. Cordero, A. Damiani, A. Malhotra, G. Seckmeyer, and P. Llanillo, 2021: Warming events projected to become more frequent and last longer across Antarctica. *Sci. Rep.*, **11**, 19564, https://doi.org/10.1038/s41598-021-98619-z.

Fogt, R. L., D. H. Bromwich, and K. M. Hines, 2011: Understanding the SAM influence on the South Pacific ENSO teleconnection. *Climate Dyn.*, **36**, 1555–1576, https://doi.org/10.1007/s00382-010-0905-0.

——, J. M. Jones, and J. Renwick, 2012: Seasonal zonal asymmetries in the Southern Annular Mode and their impact on regional temperature anomalies. *J. Climate*, **25**, 6253–6270, https://doi.org/10.1175/JCLI-D-11-00474.1.

Genthon, C., D. Six, V. Favier, M. Lazzara, and L. Keller, 2011: Atmospheric temperature measurement biases on the Antarctic Plateau. *J. Atmos. Oceanic Technol.*, **28**, 1598–1605, https://doi.org/10.1175/JTECH-D-11-00095.1.

Gilbert, E., and C. Kittel, 2021: Surface melt and runoff on Antarctic ice shelves at 1.5°C, 2°C, and 4°C of future warming. *Geophys. Res. Lett.*, **48**, e2020GL091733, https://doi.org/10.1029/2020GL091733.

——, A. Orr, J. King, I. Renfrew, T. Lachlan-Cope, P. Field, and I. Boutle, 2020: Summertime cloud phase strongly influences surface melting on the Larsen C ice shelf Antarctica. *Quart. J. Roy. Meteor. Soc.*, **146**, 1575–1589, https://doi.org/10.1002/qj.3753.

——, ——, I. A. Renfrew, J. C. King, and T. Lachlan-Cope, 2022: A 20-year study of melt processes over Larsen C Ice Shelf using a high-resolution regional atmospheric model: 2. Drivers of surface melting. *J. Geophys. Res. Atmos.*, **127**, e2021JD036012, https://doi.org/10.1029/2021JD036012.

Glasser, N. F., T. A. Scambos, J. Bohlander, M. Truffer, E. Pettit, and B. J. Davies, 2011: From ice-shelf tributary to tidewater glacier: Continued rapid recession, acceleration and thinning of Röhss Glacier following the 1995 collapse of the Prince Gustav Ice Shelf, Antarctic Peninsula. *J. Glaciol.*, **57**, 397–406, https://doi.org/10.3189/002214311796905578.

Goyal, R., M. Jucker, A. Sen Gupta, H. H. Hendon, and M. H. England, 2021: Zonal wave 3 pattern in the Southern Hemisphere generated by tropical convection. *Nat. Geosci.*, **14**, 732–738, https://doi.org/10.1038/s41561-021-00811-3.

Gutiérrez, J. M., and Coauthors, 2021: Atlas. *Climate Change 2021: The Physical Science Basis*, V. Masson-Delmotte et al., Eds., Cambridge University Press, 1927–2058.

Gutowski, W. J., Jr., and Coauthors, 2016: WCRP COordinated Regional Downscaling EXperiment (CORDEX): A diagnostic MIP for CMIP6. *Geosci. Model Dev.*, **9**, 4087–4095, https://doi.org/10.5194/gmd-9-4087-2016.

Hansen, N., S. B. Simonsen, F. Boberg, C. Kittel, A. Orr, N. Souverijns, J. M. van Wessem, and R. Mottram, 2022: Brief communication: Impact of common ice mask in surface mass balance estimates over the Antarctic ice sheet. *Cryosphere*, **16**, 711–718, https://doi.org/10.5194/tc-16-711-2022.

Heinemann, G., L. Glaw, and S. A. Willmes, 2019: Satellite-based climatology of wind-induced surface temperature anomalies for the Antarctic. *Remote Sens.*, **11**, 1539, https://doi.org/10.3390/rs11131539.

Hersbach, H., and Coauthors, 2020: The ERA5 global reanalysis. *Quart. J. Roy. Meteor. Soc.*, **146**, 1999–2049, https://doi.org/10.1002/qj.3803.

Hock, R., 2005: Glacier melt: A review of processes and their modelling. *Prog. Phys. Geogr. Earth Environ.*, **29**, 362–391, https://doi.org/10.1191/0309133305pp453ra.

Hosking, J. S., A. Orr, G. J. Marshall, J. Turner, and T. Phillips, 2013: The influence of the Amundsen-Bellingshausen Sea low on the climate of West Antarctica and its representation in coupled climate model simulations. *J. Climate*, **26**, 6633–6648, https://doi.org/10.1175/JCLI-D-12-00813.1.

Huang, B., C.-S. Shin, J. Shukla, L. Marx, M. A. Balmaseda, S. Halder, P. Dirmeyer, and J. L. Kinter III, 2017a: Reforecasting the ENSO events in the past 57 years (1958–2014). *J. Climate*, **30**, 7669–7693, https://doi.org/10.1175/JCLI-D-16-0642.1.

——, and Coauthors, 2017b: NOAA Extended Reconstructed Sea Surface Temperature (ERSST), version 5. NOAA National Centers for Environmental Information, accessed 27 August 2021, https://doi.org/10.7289/V5T72FNM.

——, C. Liu, V. Banzon, E. Freeman, G. Graham, B. Hankins, T. Smith, and H.-M. Zhang, 2021: Improvements of the Daily Optimum Interpolation Sea Surface Temperature (DOISST) version 2.1. *J. Climate*, **34**, 2923–2939, https://doi.org/10.1175/JCLI-D-20-0166.1.

Jakobs, C. L., C. H. Reijmer, M. R. van den Broeke, W. J. van de Berg, and J. M. van Wessem, 2021: Spatial variability of the snowmelt-albedo feedback in Antarctica. *J. Geophys. Res. Earth Surf.*, **126**, e2020JF005696, https://doi.org/10.1029/2020JF005696.

Jenkins, A., P. Dutrieux, S. S. Jacobs, S. D. McPhail, J. R. Perrett, A. T. Webb, and D. White, 2010: Observations beneath Pine Island Glacier in West Antarctica and implications for its retreat. *Nat. Geosci.*, **3**, 468–472, https://doi.org/10.1038/ngeo890.

——, ——, S. Jacobs, E. J. Steig, G. H. Gudmundsson, J. Smith, and K. J. Heywood, 2016: Decadal ocean forcing and Antarctic ice sheet response: Lessons from the Amundsen Sea. *Oceanography*, **29**, 106–117, https://doi.org/10.5670/oceanog.2016.103.

Johnson, A., R. Hock, and M. Fahnestock, 2022: Spatial variability and regional trends of Antarctic Ice Shelf surface melt duration over 1979–2020 derived from passive microwave data. *J. Glaciol.*, **68**, 533–546, https://doi.org/10.1017/jog.2021.112.

Karoly, D. J., 1989: Southern Hemisphere circulation features associated with El Nino-Southern Oscillation events. *J. Climate*, **2**, 1239–1252, https://doi.org/10.1175/1520-0442(1989)002<1239:SHCFAW>2.0.CO;2.

King, J. C., and Coauthors, 2015: Validation of the summertime surface energy budget of Larsen C Ice Shelf (Antarctica) as represented in three high-resolution atmospheric models. *J. Geophys. Res. Atmos.*, **120**, 1335–1347, https://doi.org/10.1002/2014JD022604.

Kingslake, J., J. C. Ely, I. Das, and R. E. Bell, 2017: Widespread movement of meltwater onto and across Antarctic ice shelves. *Nature*, **544**, 349–352, https://doi.org/10.1038/nature22049.

Krinner, G., and C. Genthon, 1999: Altitude dependence of the ice sheet surface climate. *Geophys. Res. Lett.*, **26**, 2227–2230, https://doi.org/10.1029/1999GL900536.

Kuipers Munneke, P., M. R. van den Broeke, J. C. King, T. Gray, and C. H. Reijmer, 2012: Near-surface climate and surface energy budget of Larsen C Ice Shelf, Antarctic Peninsula. *Cryosphere*, **6**, 353–363, https://doi.org/10.5194/tc-6-353-2012.

——, and Coauthors, 2018: Intense winter surface melt on an Antarctic Ice Shelf. *Geophys. Res. Lett.*, **45**, 7615–7623, https://doi.org/10.1029/2018GL077899.

Laffin, M. K., C. S. Zender, S. Singh, J. M. van Wessem, C. J. P. P. Smeets, and C. H. Reijmer, 2021: Climatology and evolution of the Antarctic Peninsula föhn wind–induced melt regime from 1979–2018. *J. Geophys. Res. Atmos.*, **126**, e2020JD033682, https://doi.org/10.1029/2020JD033682.

Lai, C.-Y., J. Kingslake, M. G. Wearing, P.-H. Cameron Chen, P. Gentine, H. Li, J. J. Spergel, and J. M. van Wessem, 2020: Vulnerability of Antarctica's ice shelves to meltwater-driven fracture. *Nature*, **584**, 574–578, https://doi.org/10.1038/s41586-020-2627-8.

Lazzara, M. A., G. A. Weidner, L. M. Keller, J. E. Thom, and J. J. Cassano, 2012: Antarctic Automatic Weather Station Program: 30 years of polar observation. *Bull. Amer. Meteor. Soc.*, **93**, 1519–1537, https://doi.org/10.1175/BAMS-D-11-00015.1.

Lenaerts, J. T. M., and Coauthors, 2017: Meltwater produced by wind–albedo interaction stored in an East Antarctic Ice Shelf. *Nat. Climate Change*, **7**, 58–62, https://doi.org/10.1038/nclimate3180.

——, and Coauthors, 2018: Climate and surface mass balance of coastal West Antarctica resolved by regional climate modelling. *Ann. Glaciol.*, **59**, 29–41, https://doi.org/10.1017/aog.2017.42.

L'Heureux, M. L., and D. W. J. Thompson, 2006: Observed relationships between the El Nino–Southern Oscillation and the extratropical zonal-mean circulation. *J. Climate*, **19**, 276–287, https://doi.org/10.1175/JCLI3617.1.

Liebmann, B., and C. A. Smith, 1996: Description of a complete (interpolated) outgoing longwave radiation dataset. *Bull. Amer. Meteor. Soc.*, **77**, 1275–1277, https://doi.org/10.1175/1520-0477-77.6.1274.

Liston, G. E., and J.-G. Winther, 2005: Antarctic surface and subsurface snow and ice melt fluxes. *J. Climate*, **18**, 1469–1481, https://doi.org/10.1175/JCLI3344.1.

Lo, J. C.-F., Z.-L. Yang, and R. A. Pielke Sr., 2008: Assessment of three dynamical climate downscaling methods using the Weather Research and Forecasting (WRF) Model. *J. Geophys. Res.*, **113**, D09112, https://doi.org/10.1029/2007JD009216.

Luckman, A., A. Elvidge, D. Jansen, B. Kulessa, P. Kuipers Munneke, J. King, and N. E. Barrand, 2014: Surface melt and ponding on Larsen C Ice Shelf and the impact of föhn winds. *Antarct. Sci.*, **26**, 625–635, https://doi.org/10.1017/S0954102014000339.

MacAyeal, D. R., T. A. Scambos, C. L. Hulbe, and M. A. Fahnestock, 2003: Catastrophic ice-shelf break-up by an ice-shelf-fragment-capsize mechanism. *J. Glaciol.*, **49**, 22–36, https://doi.org/10.3189/172756503781830863.

Mann, H. B., 1945: Non parametric test against trend. *Econometric*, **13**, 245–259, https://doi.org/10.2307/1907187.

Marshall, G. J., 2003: Trends in the Southern Annular Mode from observations and reanalyses. *J. Climate*, **16**, 4134–4143, https://doi.org/10.1175/1520-0442(2003)016<4134:TITSAM>2.0.CO;2.

——, 2018: The climate data guide: Marshall Southern Annular Mode (SAM) index (station-based). NCAR, accessed 14 December 2021, https://climatedataguide.ucar.edu/climate-data/marshall-southern-annular-mode-sam-index-station-based.

Mottram, R., and Coauthors, 2021: What is the surface mass balance of Antarctica? An intercomparison of regional climate model estimates. *Cryosphere*, **15**, 3751–3784, https://doi.org/10.5194/tc-15-3751-2021.

Mouginot, J., E. Rignot, and B. Scheuchl, 2017: MEaSUREs Antarctic Boundaries for IPY 2007–2009 from Satellite Radar, version 1. NASA National Snow and Ice Data Center Distributed Active Archive Center, accessed 14 December 2021, https://doi.org/10.5067/SEVV4MR8P1ZN.

Nicolas, J. P., and D. H. Bromwich, 2011: Climate of West Antarctica and influence of marine air intrusions. *J. Climate*, **24**, 49–67, https://doi.org/10.1175/2010JCLI3522.1.

——, and Coauthors, 2017: January 2016 extensive summer melt in West Antarctica favoured by strong El Niño. *Nat. Commun.*, **8**, 15799, https://doi.org/10.1038/ncomms15799.

Ohmura, A., 2001: Physical basis for the temperature-based melt-index method. *J. Appl. Meteor.*, **40**, 753–761, https://doi.org/10.1175/1520-0450(2001)040<0753:PBFTTB>2.0.CO;2.

Orr, A., D. Cresswell, G. J. Marshall, J. C. R. Hunt, J. Sommeria, C. G. Wang, and M. Light, 2004: A 'low-level' explanation for the recent large warming trend over the western Antarctic Peninsula involving blocked winds and changes in zonal circulation. *Geophys. Res. Lett.*, **31**, L06204, https://doi.org/10.1029/2003GL019160.

——, G. J. Marshall, J. C. R. Hunt, J. Sommeria, C.-G. Wang, N. P. M. van Lipzig, D. Cresswell, and J. C. King, 2008: Characteristics of airflow over the Antarctic Peninsula and its response to recent strengthening of westerly circumpolar winds. *J. Atmos. Sci.*, **65**, 1396–1413, https://doi.org/10.1175/2007JAS2498.1.

——, T. Phillips, S. Webster, A. Elvidge, M. Weeks, S. Hosking, and J. Turner, 2014: Met Office Unified Model high resolution simulations of a strong wind event in Antarctica. *Quart. J. Roy. Meteor. Soc.*, **140**, 2287–2297, https://doi.org/10.1002/qj.2296.

——, and Coauthors, 2021: Comparison of kilometre and sub-kilometre scale simulations of a Foehn wind event over the Larsen C Ice Shelf, Antarctic Peninsula using the Met Office Unified Model (MetUM). *Quart. J. Roy. Meteor. Soc.*, **147**, 3472–3492, https://doi.org/10.1002/qj.4138.

Paolo, F. S., H. A. Fricker, and L. Padman, 2015: Volume loss from Antarctic ice shelves is accelerating. *Science*, **348**, 327–331, https://doi.org/10.1126/science.aaa0940.

Parish, T. R., and D. H. Bromwich, 1989: Instrumented aircraft observations of the katabatic wind regime near Terra Nova Bay. *Mon. Wea. Rev.*, **117**, 1570–1585, https://doi.org/10.1175/1520-0493(1989)117<1570:IAOOTK>2.0.CO;2.

——, and ——, 1991: Continental-scale simulation of the Antarctic katabatic wind regime. *J. Climate*, **4**, 135–146, https://doi.org/10.1175/1520-0442(1991)004<0135:CSSOTA>2.0.CO;2.

——, J. J. Cassano, and M. W. Seefeldt, 2006: Characteristics of the Ross Ice Shelf air stream as depicted in Antarctic Meso-scale Prediction System simulations. *J. Geophys. Res.*, **111**, D12109, https://doi.org/10.1029/2005JD006185.

Picard, G., M. Fily, and H. Gallee, 2007: Surface melting derived from microwave radiometers: A climatic indicator in Antarctica. *Ann. Glaciol.*, **46**, 29–34, https://doi.org/10.3189/172756407782871684.

Power, S., F. Delage, C. Chung, G. Kociuba, and K. Keay, 2013: Robust twenty-first-century projections of El Niño and related precipitation variability. *Nature*, **502**, 541–545, https://doi.org/10.1038/nature12580.

Pritchard, H. D., S. R. M. Ligtenberg, H. A. Fricker, D. G. Vaughan, M. R. van den Broeke, and L. Padman, 2012: Antarctic ice-sheet loss driven by basal melting of ice shelves. *Nature*, **484**, 502–505, https://doi.org/10.1038/nature10968.

Purich, A., and Coauthors, 2016: Tropical Pacific SST drivers of recent Antarctic Sea ice trends. *J. Climate*, **29**, 8931–8948, https://doi.org/10.1175/JCLI-D-16-0440.1.

Rignot, E., J. Mouginot, B. Scheuchl, M. van den Broeke, M. J. van Wessem, and M. Morlighem, 2019: Four decades of Antarctic Ice Sheet mass balance from 1979–2017. *Proc. Natl. Acad. Sci. USA*, **116**, 1095–1103, https://doi.org/10.1073/pnas.1812883116.

Rott, H., P. Skvarca, and T. Nagler, 1996: Rapid collapse of northern Larsen Ice Shelf, Antarctica. *Science*, **271**, 788–792, https://doi.org/10.1126/science.271.5250.788.

Santoso, A., S. McGregor, F.-F. Jin, W. Cai, M. H. England, S.-I. An, M. J. McPhaden, and E. Guilyardi, 2013: Late-twentieth-century emergence of the El Niño propagation asymmetry and future projections. *Nature*, **504**, 126–130, https://doi.org/10.1038/nature12683.

Scambos, T. A., C. Hulbe, M. Fahnestock, and J. Bohlander, 2000: The link between climate warming and break-up of ice shelves in the Antarctic Peninsula. *J. Glaciol.*, **46**, 516–530, https://doi.org/10.3189/172756500781833043.

——, H. A. Fricker, C.-C. Liu, J. Bohlander, J. Fastook, A. Sargent, R. Massom, and A.-M. Wu, 2009: Ice shelf disintegration by plate bending and hydro-fracture: Satellite observations and model results of the 2008 Wilkins Ice Shelf break-ups. *Earth Planet. Sci. Lett.*, **280**, 51–60, https://doi.org/10.1016/j.epsl.2008.12.027.

Scott, R. C., J. P. Nicolas, D. H. Bromwich, J. R. Norris, and D. Lubin, 2019: Meteorological drivers and large-scale climate forcing on West Antarctic surface melt. *J. Climate*, **32**, 665–684, https://doi.org/10.1175/JCLI-D-18-0233.1.

Scott Yiu, Y. Y., and A. C. Maycock, 2019: On the seasonality of the El Niño teleconnection to the Amundsen Sea region. *J. Climate*, **32**, 4829–4845, https://doi.org/10.1175/JCLI-D-18-0813.1.

Seefeldt, M. W., and J. J. Cassano, 2008: An analysis of low-level jets in the greater Ross Ice Shelf region based on numerical simulations. *Mon. Wea. Rev.*, **136**, 4188–4205, https://doi.org/10.1175/2008MWR2455.1.

——, and ——, 2012: A description of the Ross Ice Shelf air stream (RAS) through the use of Self-Organizing Maps (SOMs). *J. Geophys. Res.*, **117**, D09112, https://doi.org/10.1029/2011JD016857.

Simmonds, I., and K. Keay, 2000a: Mean Southern Hemisphere extratropical cyclone behavior in the 40-year NCEP–NCAR reanalysis. *J. Climate*, **13**, 873–885, https://doi.org/10.1175/1520-0442(2000)013<0873:MSHECB>2.0.CO;2.

——, and ——, 2000b: Variability of Southern Hemisphere extratropical cyclone behavior, 1958–97. *J. Climate*, **13**, 550–561, https://doi.org/10.1175/1520-0442(2000)013<0550:VOSHEC>2.0.CO;2.

Speirs, J. C., D. F. Steinhoff, H. A. McGowan, D. H. Bromwich, and A. J. Monaghan, 2010: Foehn winds in the McMurdo dry valleys, Antarctica: The origin of extreme warming events. *J. Climate*, **23**, 3577–3598, https://doi.org/10.1175/2010JCLI3382.1.

Stokes, C. R., J. E. Sanderson, B. W. J. Miles, S. S. R. Jamieson, and A. A. Leeson, 2019: Widespread distribution of supraglacial lakes around the margin of the East Antarctic Ice Sheet. *Sci. Rep.*, **9**, 13823, https://doi.org/10.1038/s41598-019-50343-5.

Takaya, K., and H. Nakamura, 2001: A formulation of a phase-independent wave-activity flux for stationary and migratory quasigeostrophic eddies on a zonally varying basic flow. *J. Atmos. Sci.*, **58**, 608–627, https://doi.org/10.1175/1520-0469(2001)058<0608:AFOAPI>2.0.CO;2.

Tedesco, M., 2009: Assessment and development of snowmelt retrieval algorithms over Antarctica from K-band spaceborne brightness temperature (1979–2008). *Remote Sens. Environ.*, **113**, 979–997, https://doi.org/10.1016/j.rse.2009.01.009.

——, W. Abdalati, and H. J. Zwally, 2007: Persistent surface snowmelt over Antarctica (1987–2006) from 19.35 GHz brightness temperatures. *Geophys. Res. Lett.*, **34**, L18504, https://doi.org/10.1029/2007GL031199.

Trusel, L. D., K. E. Frey, and S. B. Das, 2012: Antarctic surface melting dynamics: Enhanced perspectives from radar scatterometer data. *J. Geophys. Res.*, **117**, F02023, https://doi.org/10.1029/2011JF002126.

——, ——, ——, P. Kuipers Munneke, and M. R. van den Broeke, 2013: Satellite-based estimates of Antarctic surface meltwater fluxes. *Geophys. Res. Lett.*, **40**, 6148–6153, https://doi.org/10.1002/2013GL058138.

——, ——, ——, K. B. Karnauskas, P. Kuipers Munneke, E. van Meijgaard, and M. R. van den Broeke, 2015: Divergent trajectories of Antarctic surface melt under two twenty-first-century climate scenarios. *Nat. Geosci.*, **8**, 927–932, https://doi.org/10.1038/ngeo2563.

Turner, J., and Coauthors, 2016: Absence of 21st century warming on Antarctic Peninsula consistent with natural variability. *Nature*, **535**, 411–415, https://doi.org/10.1038/nature18645.

——, H. Lu, J. King, G. J. Marshall, T. Phillips, D. Bannister, and S. Colwell, 2021: Extreme temperatures in the Antarctic. *J. Climate*, **34**, 2653–2668, https://doi.org/10.1175/JCLI-D-20-0538.1.

van den Broeke, M., C. Bus, J. Ettema, and P. Smeets, 2010: Temperature thresholds for degree-day modelling of Greenland ice sheet melt rates. *Geophys. Res. Lett.*, **37**, L18501, https://doi.org/10.1029/2010GL044123.

van Wessem, J. M., C. H. Reijmer, J. T. M. Lenaerts, W. J. van de Berg, M. R. van den Broeke, and E. van Meijgaard, 2014: Updated cloud physics in a regional atmospheric climate model improves the modelled surface energy balance of Antarctica. *Cryosphere*, **8**, 125–135, https://doi.org/10.5194/tc-8-125-2014.

Walters, D., and Coauthors, 2017: The Met Office Unified Model Global Atmosphere 6.0/6.1 and JULES Global Land 6.0/6.1 configurations. *Geosci. Model Dev.*, **10**, 1487–1520, https://doi.org/10.5194/gmd-10-1487-2017.

——, and Coauthors, 2019: The Met Office Unified Model Global Atmosphere 7.0/7.1 and JULES Global Land 7.0 configurations. *Geosci. Model Dev.*, **12**, 1909–1963, https://doi.org/10.5194/gmd-12-1909-2019.

Wei, T., Q. Yan, and M. Ding, 2019: Distribution and temporal trends of temperature extremes over Antarctica. *Environ. Res. Lett.*, **14**, 084040, https://doi.org/10.1088/1748-9326/ab33c1.

Wille, J. D., V. Favier, A. Dufour, I. V. Gorodetskaya, J. Turner, C. Agosta, and F. Codron, 2019: West Antarctic surface melt triggered by atmospheric rivers. *Nat. Geosci.*, **12**, 911–916, https://doi.org/10.1038/s41561-019-0460-1.

——, and Coauthors, 2021: Antarctic atmospheric river climatology and precipitation impacts. *J. Geophys. Res. Atmos.*, **126**, e2020JD033788, https://doi.org/10.1029/2020JD033788.

——, and Coauthors, 2022: Intense atmospheric rivers can weaken ice shelf stability at the Antarctic Peninsula. *Commun. Earth Environ.*, **3**, 90, https://doi.org/10.1038/s43247-022-00422-9.

Wilson, A. B., D. H. Bromwich, and K. M. Hines, 2012: Evaluation of Polar WRF forecasts on the Arctic System Reanalysis Domain: 2. Atmospheric hydrologic cycle. *J. Geophys. Res.*, **117**, D04107, https://doi.org/10.1029/2011JD016765.

Zheng, F., J. Li, R. T. Clark, and H. C. Nnamchi, 2013: Simulation and projection of the Southern Hemisphere annular mode in CMIP5 models. *J. Climate*, **26**, 9860–9879, https://doi.org/10.1175/JCLI-D-13-00204.1.

Zou, X., D. H. Bromwich, A. Montenegro, S.-H. Wang, and L. Bai, 2021: Major surface melting over the Ross Ice Shelf Part I: Foehn effect. *Quart. J. Roy. Meteor. Soc.*, **147**, 2874–2894, https://doi.org/10.1002/qj.4104.